

ARTICLE TYPE

Multiscale modeling of linear elastic heterogeneous structures via localized model order reduction

Philipp Diercks^{*1} | Karen Veroy² | Annika Robens-Radermacher¹ | Jörg F. Unger¹

¹Department 7.7 Modeling and Simulation, Bundesanstalt für Materialforschung und -prüfung (BAM), Unter den Eichen 87, 12205 Berlin, Germany

²Centre for Analysis, Scientific Computing and Applications (CASA) Department of Mathematics and Computer Science, University of Eindhoven, P.O. Box 513, 5600 MB Eindhoven, The Netherlands

Correspondence

*Philipp Diercks, Unter den Eichen 87, 12205 Berlin, Germany, Email: philipp.diercks@bam.de

Present Address

Unter den Eichen 87, 12205 Berlin, Germany

Abstract

In analyzing large scale structures it is necessary to take into account the fine scale heterogeneity for accurate failure prediction. Resolving fine scale features in the numerical model drastically increases the number of degrees of freedom, thus making full fine-scale simulations infeasible, especially in cases where the model needs to be evaluated many times.

In this paper, a methodology for fine scale modeling of large scale structures is proposed, which combines the variational multiscale method, domain decomposition and model order reduction. To address applications where the assumption of scale separation does not hold, the influence of the fine scale on the coarse scale is modelled directly by the use of an additive split of the displacement field. Possible coarse and fine scale solutions are exploited for a representative coarse grid element (RCE) to construct local approximation spaces. The local spaces are designed such that local contributions of RCE subdomains can be coupled in a conforming way. Therefore, the resulting global system of equations takes the effect of the fine scale on the coarse scale into account, is sparse and reduced in size compared to the full order model. Several numerical experiments show the accuracy and efficiency of the method.

KEYWORDS:

Multiscale methods; variational multiscale method; localized model order reduction; proper orthogonal decomposition; domain decomposition methods

1 | INTRODUCTION

1.1 | Multiscale modeling and model order reduction

Many problems in science and engineering involve multiple scales. With large disparities present in spatial or temporal scales, it is often insufficient to assume a homogeneous material in the analysis of a mechanical structure. For example, the dispersed phases (particles or fibers) in a composite material may lead to fluctuations in the displacement field which cannot be captured by the phenomenological macroscale model. Therefore, in analyzing large scale structures, it is necessary to take into account the materials' fine scale heterogeneity to more accurately model the structure's behaviour.

It is often sufficient to predict macroscopic properties of the multiscale system based on a representative volume element (RVE), that preserves the geometrical complexity of the heterogeneous microstructure and accurately predicts effective material parameters. Approaches based on computational homogenization, such as the FE² method (see e. g. ^{1,2,3,4}) mitigate the issue of computational cost compared to full fine scale simulations, but the nested solution procedure is still a demanding task. Therefore,

many approaches^{5,6,7,8} combining the FE^2 approach with model reduction of the fine scale problem exist. These approaches rest on the assumption of *separation of scales* and the existence of an RVE; however, this is not the case in many applications, e. g. in the presence of macroscopic cracks emerging from the localization of microdefects^{9,10}.

Thus, methods which address both scales simultaneously are needed. Standard multiscale methods have emerged from the variational approaches to numerical homogenization, such as the variational multiscale method (VMM)^{11,12} or the multiscale finite element method (MsFEM)¹³, which aim for a correction or stabilization of the conventional (coarse grid) discretization by including (unresolved) fine scale information into the global problem. Important developments of the VMM include the works by M. Larson and A. Målqvist^{14,15,16} and the local orthogonal decomposition (LOD)¹⁷. For a more detailed discussion on the history of numerical homogenization in the absence of a clear separation of scales we refer to Altmann et al.¹⁸.

In addition, the significant increase in computational cost entailed with the resolution of the fine scale features in the numerical model necessitates the use of model order reduction techniques (see the textbooks^{19,20} for an introduction to the topic). The high dimensional numerical problem (also termed high-fidelity approximation or full order model (FOM)) is replaced by a reduced order model (ROM) of small dimension, which is achieved by the projection of the original system of equations upon a subspace of the solution manifold. A key point is the construction of the reduced basis, which spans the low dimensional subspace, from a set of suitably selected high-fidelity solutions. In (now standard) reduced basis (RB) methods, the so-called snapshots are selected via the weak greedy algorithm^{21,22}. Another popular method for subspace construction is the proper orthogonal decomposition (POD)^{23,24}. However, efficient reduction of nonlinear problems in mechanics still poses a challenge due to the repeated evaluation of the weak form over the full domain. Among others, well-known techniques to address this issue are the empirical interpolation method (EIM)²⁵ and its discrete variant²⁶, the hyper-reduction^{27,28}, the energy-conserving sampling and weighting method^{29,30} or the empirical cubature method³¹. Moreover, more recent approaches^{32,33} make use of machine learning methods to construct ROMs for nonlinear problems.

However, in the case of full fine scale simulations, limitations of established model order reduction techniques become apparent; examples of such limitations include prohibitively large reduced spaces due to high dimensional parameter spaces or computationally expensive offline phases due to large computational domains. To alleviate these shortcomings, methods combining multiscale methods, domain decomposition and model order reduction were developed. Approaches of this kind are known as *localized model order reduction methods*, and an extensive review is given by Buhr et al.³⁴. The main idea is the construction of local reduced spaces on subdomains, i. e. parts of the global domain, which are then coupled (either in a conforming or non-conforming way) to obtain a global approximation.

1.2 | Contributions and relation to previous work

In this work, we aim to provide a computationally efficient framework for multiscale modeling of heterogeneous structures that is able to incorporate localization phenomena as described in section 1.1. Therefore, we suggest an approach that addresses both scales simultaneously and is flexible enough to adaptively incorporate complex nonlinear material behaviour. Since the approximation of e. g. a propagating crack does not work well with existing reduction techniques, we envision an approach in which the localization is represented only up to a certain point and it is able to adaptively move to a full order model in certain parts of the domain. In this contribution, we provide the basis for such a framework, whereas the extension to the nonlinear case is planned as future work.

The proposed methodology features an additive split of the displacement field into coarse and fine scale parts, based on the VMM. The coarse scale basis functions are computed directly by extending standard finite element shape functions on the boundary of local subdomains into the interior of the respective subdomains. Local approximation spaces for the fine scale part are constructed by exploiting possible fine scale solutions for a representative coarse grid element (RCE) using the concept of oversampling first introduced in the context of the MsFEM¹³. To this end, a so-called transfer eigenvalue problem^{35,36} (or oversampling problem) yielding local reduced spaces which are optimal in the sense of Kolmogorov is solved and the associated transfer operator is approximated by random sampling³⁷. In addition, algorithm 1 of³⁷ is modified to inform the boundary conditions of the oversampling problem by the solution of a reduced global problem. Note that a similar approach to build local reduced spaces using interface basis functions (Lagrangian or Fourier bases) as boundary conditions was proposed in Iapichino et al.³⁸. The difference is that Iapichino et al. prescribed these interface basis functions on the boundary of the subdomain of interest directly. In our approach, the (macroscopic) displacement state of the global structure of interest is prescribed on the boundary of the oversampling domain using coarse finite element shape functions, making it more suitable for the construction of reduced spaces tailored to the solution of the partial differential equation (PDE) in that area of the domain. Moreover, we further

restrict the fine scale solutions obtained from the oversampling problem to the edges of the target subdomain and by means of POD, construct a reduced fine scale edge basis. Then, the fine scale edge basis functions are again extended into the interior of the subdomain. We note that such a procedure to construct a conforming, localized reduced order approximation is outlined in a more general form in the review by Buhr et al.³⁴. Finally, the fine scale subdomain basis functions are problem-dependent local functions which are continuous on subdomain boundaries and thus yield a conforming approximation. This decomposition of the fine scale part in its respective edge parts is favorable since the resulting discrete equation system of the (global) ROM preserves the sparsity pattern and computational complexity of standard finite element methods.

As an alternative to the decomposition outlined above, the generalized finite element method (GFEM)^{39,40,41} can be used to construct a global approximation from local reduced spaces. To this end, local reduced basis functions are multiplied with standard finite element shape functions to create a partition of unity. This thus leads to a larger number of degrees of freedom in the resulting global approximation compared to the approach proposed in this work.

In view of the extension of the method to the nonlinear case, we expect that the impact of incorporating the local deformation state of the structure of interest in the construction of the local reduced basis will be more significant. Also, the amplitude of the boundary conditions prescribed in the oversampling problem is relevant in the nonlinear case which may be challenging in the case of random boundary conditions. Due to the resemblance of the constructed empirical fine scale basis functions with hierarchical FE shape functions (see e.g.⁴²), it is then possible to incorporate strategies from the field of adaptive refinement (p -refinement).

The remainder of this article is organised as follows. First, in section 2, the problem setting and full order model are described. The proposed method is explained in section 3, comprising the construction of local approximation spaces in section 3.1 and the assembly of the reduced order model in section 3.2. Numerical examples illustrating the performance of the suggested approach are discussed in section 4. Concluding remarks and an outlook are given in section 5.

2 | PROBLEM SETTING AND MODELING

While the method could be applied to other PDEs, only the balance of linear momentum in the static case on a large computational domain $\Omega_{\text{gl}} \subset \mathbb{R}^d$ (the suffix ‘gl’ stands for global) is considered, with boundary $\partial\Omega_{\text{gl}} = \Sigma_{\text{N}} \cup \Sigma_{\text{D}}$, where Σ_{N} and Σ_{D} denote Neumann and Dirichlet boundaries, respectively, and $d = 2, 3$ is the spatial dimension. Without loss of generality, volumetric forces are neglected, and the displacement solution \mathbf{u}_{gl} is sought such that

$$\begin{aligned} -\nabla \cdot \boldsymbol{\sigma}(\nabla \mathbf{u}_{\text{gl}}) &= 0 \quad \text{in } \Omega_{\text{gl}}, \\ \boldsymbol{\sigma}(\nabla \mathbf{u}_{\text{gl}}) \cdot \mathbf{n} &= \hat{\mathbf{t}} \quad \text{on } \Sigma_{\text{N}}, \\ \mathbf{u}_{\text{gl}} &= \mathbf{g}_{\text{D}} \quad \text{on } \Sigma_{\text{D}}. \end{aligned} \quad (1)$$

Here the Cauchy stress tensor $\boldsymbol{\sigma}$ for one of the M material components of the heterogeneous linear elastic material is given by

$$\boldsymbol{\sigma}_m = \lambda_m^1 (\varepsilon(\mathbf{u}_{\text{gl}}) \cdot \cdot \mathbb{1}) \mathbb{1} + 2\lambda_m^2 \varepsilon(\mathbf{u}_{\text{gl}}), \quad \text{with } m = 1, \dots, M, \quad (2)$$

where λ_m^1 and λ_m^2 are Lamé’s constants. The linear strain operator is denoted by $\varepsilon(\mathbf{v}) = \frac{1}{2} (\nabla \mathbf{v} + \nabla \mathbf{v}^T)$. Moreover, \mathbf{n} is the body’s surface outward normal vector, $\hat{\mathbf{t}}$ is the traction given on the Neumann boundary Σ_{N} and $\hat{\mathbf{u}}$ is the displacement prescribed on the Dirichlet boundary Σ_{D} . We define $\mathbf{u}_{\text{gl}} = \mathbf{u}_0 + \mathbf{u}_{\text{D}}$, with a suitable *dirichlet lift* $\mathbf{u}_{\text{D}} \in \mathbb{V}_{\text{D}} = \{\mathbf{v} \in [H^1(\Omega_{\text{gl}})]^d : \mathbf{v} = \mathbf{g}_{\text{D}} \text{ on } \Sigma_{\text{D}}\}$ in case of inhomogeneous Dirichlet boundary conditions. The weak form for eq. (1) reads: find $\mathbf{u}_0 \in \mathbb{V} = \{\mathbf{v} \in [H^1(\Omega_{\text{gl}})]^d : \mathbf{v} = \mathbf{0} \text{ on } \Sigma_{\text{D}}\}$ such that

$$a(\mathbf{u}_{\text{gl}}, \mathbf{v}) = f(\mathbf{v}), \quad \forall \mathbf{v} \in \mathbb{V}, \quad (3)$$

where

$$a(\mathbf{w}, \mathbf{v}) = \sum_{m=1}^M \int_{\Omega_{\text{gl}}^m} \lambda_m^1 \text{tr}(\varepsilon(\mathbf{w})) \text{tr}(\varepsilon(\mathbf{v})) + 2\lambda_m^2 \varepsilon(\mathbf{w}) \cdot \cdot \varepsilon(\mathbf{v}) \, dV \quad (4)$$

and

$$f(\mathbf{v}) = \int_{\partial\Omega_{\text{gl}}} \hat{\mathbf{t}} \cdot \mathbf{v} \, dA - a(\mathbf{u}_{\text{D}}, \mathbf{v}). \quad (5)$$

Here, Ω_{gl}^m is used to indicate the parts of the global domain associated with the different phases of the heterogeneous material. Note that, $\text{tr}(\bullet)$ denotes the trace of a tensor and ‘ $\cdot \cdot$ ’ stands for the scalar product of two 2nd-order tensors (2-fold contraction as

defined in section 2.1.15 of⁴³). The energy inner product and energy norm are defined as

$$(\mathbf{w}, \mathbf{v})_{\mathbb{V}} = a(\mathbf{w}, \mathbf{v}), \quad \forall \mathbf{w}, \mathbf{v} \in \mathbb{V}, \quad (6)$$

$$\|\mathbf{v}\|_{\mathbb{V}}^2 = a(\mathbf{v}, \mathbf{v}), \quad \forall \mathbf{v} \in \mathbb{V}. \quad (7)$$

2.1 | Full order model

The *direct numerical solution* or *full order model* is defined as the finite element approximation of eq. (3), searching for the solution in a high fidelity discrete space $\mathbb{V}_{\delta} \subset \mathbb{V}$: find $\mathbf{u}_{\delta} \in \mathbb{V}_{\delta} \subset \mathbb{V}$, such that

$$a(\mathbf{u}_{\delta}, \mathbf{v}) = f(\mathbf{v}), \quad \forall \mathbf{v} \in \mathbb{V}_{\delta}. \quad (8)$$

The dimension of the discrete space is denoted by $N_{\delta} = \dim(\mathbb{V}_{\delta})$, and we denote by $\{\phi_i\}_{i=1}^{N_{\delta}}$ a standard finite element basis of \mathbb{V} such that, the stiffness matrix and right hand side can be written as

$$(\mathbf{A}_{\delta})_{ij} = a(\phi_j, \phi_i), \quad (\mathbf{f}_{\delta})_i = f(\phi_i). \quad (9)$$

3 | MULTISCALE METHOD

Every material is intrinsically multiscale. In the framework of continuum mechanics, often the assumption of a homogeneous material to solve macroscale problems is sufficient. However, it is only a homogenized approximation of the underlying finer scales and thus not suitable in loading conditions where the real physical phenomena on the fine scale greatly influence the macroscopic behaviour. Consider for example the propagation of a crack in the test specimen shown in fig. 1, which is only tractable by resolving the fine scale in the numerical model. The macroscopic approximation then needs to be improved by fine scale functions taking into account fluctuations in the displacement field due to the heterogeneous fine scale structure. Note that the discretization of the fine scale structure is assumed to be the same throughout the whole mesoscale structure and that we aim at a reduction of the fully resolved subdomain by construction of representative coarse grid elements (RCE), whose associated reduced basis functions are able to model both scales sufficiently. The RCE should be statistically representative such that the geometrical complexity of the heterogeneous fine scale structure is preserved, but the accurate prediction of effective material behaviour is not required since a computational homogenization ansatz is not followed.

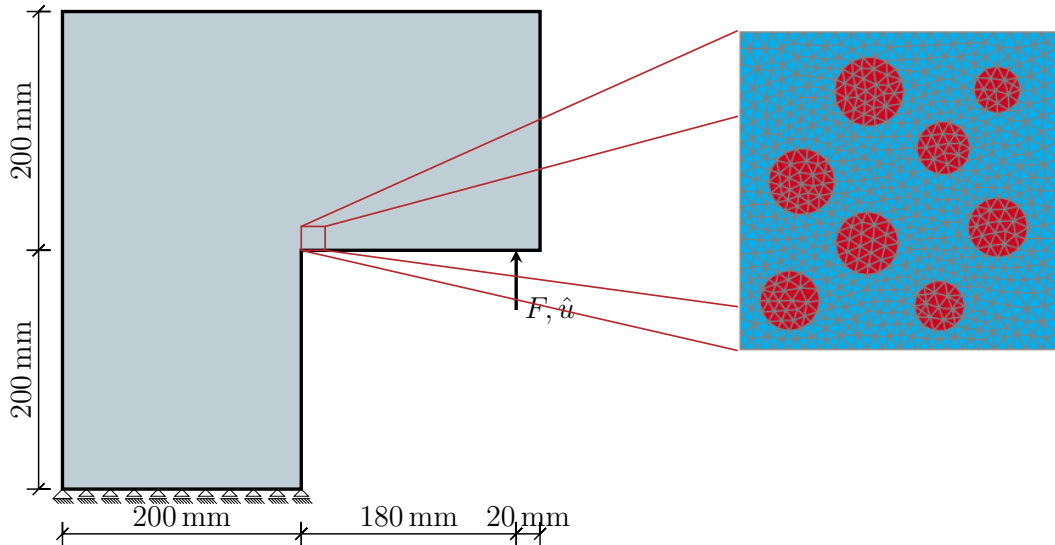


FIGURE 1 L-shaped panel test specimen and exemplary fine scale structure.

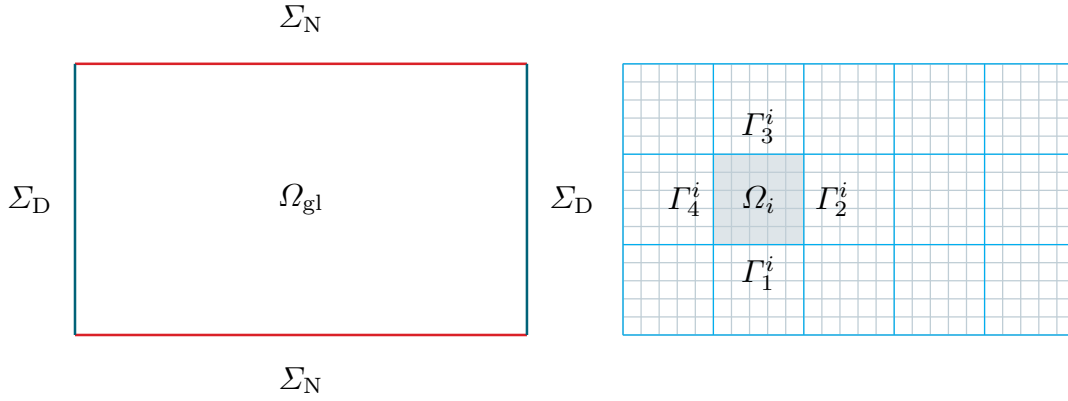


FIGURE 2 Exemplary computational domain Ω_{gl} on the left and coarse scale (blue lines) and fine scale (gray lines) grid partition on the right. A subdomain Ω_i and its edges Γ_e^i are also shown.

Following this line of thought, we introduce an additive split of the displacement solution $\mathbf{u}_0 = \mathbf{u}_c + \mathbf{u}_f$ and (in analogy to section 2) the Hilbert space

$$\mathbb{V} = \mathbb{V}_c \oplus \mathbb{V}_f, \quad (10)$$

is introduced, such that

$$a(\mathbf{u}_c, \mathbf{v}_c) + a(\mathbf{u}_f, \mathbf{v}_c) = f(\mathbf{v}_c) \quad \forall \mathbf{v}_c \in \mathbb{V}_c, \quad (11)$$

$$a(\mathbf{u}_c, \mathbf{v}_f) + a(\mathbf{u}_f, \mathbf{v}_f) = f(\mathbf{v}_f) \quad \forall \mathbf{v}_f \in \mathbb{V}_f. \quad (12)$$

Here $(\bullet)_c$ denotes the coarse scale part and $(\bullet)_f$ the fine scale part. The corresponding discrete spaces are associated with coarse scale and fine scale partitions of the domain Ω_{gl} as depicted in fig. 2. It is assumed that the global domain can be decomposed into N_c non-overlapping RCEs (i. e. subdomains) denoted by Ω_i , $i = 1, 2, \dots, N_c$. Within each RCE Ω_i , the computational domain for each of the material phases is denoted by Ω_i^m with $m = 1, \dots, M$ in analogy to the definitions in section 2. Furthermore, the subdomain boundaries are denoted by Γ_e^i , with $e = 1, 2, 3, 4$ referring to the respective bottom, right, top and left edge of the subdomain. Analogously, the global space \mathbb{V} is decomposed into subdomain spaces \mathbb{V}_i with dimension $n_\delta^i = \dim(\mathbb{V}_i)$,

$$\mathbb{V} = \bigoplus_{i=1}^{N_c} \mathbb{V}_i. \quad (13)$$

Section 3.1 deals with the construction of reduced basis functions which yield a good approximation of \mathbf{u}_{gl} , such that the PDE eq. (1) is locally fulfilled on Ω_i . The definition of the global approximation is described in section 3.2.

3.1 | Construction of local approximation spaces

In this section, the construction of the reduced basis functions for the coarse scale, $\{\boldsymbol{\varphi}_i\}_{i=1}^{n_c}$, and for the fine scale, $\{\boldsymbol{\psi}_i\}_{i=1}^{n_f}$, is addressed. The proposed *offline phase* consists of three stages:

1. direct calculation of coarse scale basis $\{\boldsymbol{\varphi}_i\}_{i=1}^{n_c}$,
2. calculation of fine scale edge basis functions $\{\boldsymbol{\chi}_i^e\}_{i=1}^{n_{\text{mpe}}}$, where n_{mpe} denotes the number of modes per (subdomain) edge; via two approaches:
 - (a) by solving an oversampling problem (leading to an *empirical* basis),
 - (b) by constructing *hierarchical* finite element shape functions h_{p+1} (see e. g. chapter 8 in ⁴²) of degree $p + 1$, where p is the polynomial degree of the Legendre polynomial $P_p(\xi)$,

$$h_{p+1} = \int P_p(\xi) d\xi, \quad \text{with } P_p(\xi) = \frac{1}{(p-1)!} \frac{1}{2^{p-1}} \frac{d^p}{d\xi^p} [(\xi^2 - 1)^p], \quad (14)$$

3. calculation of fine-scale subdomain basis functions $\{\boldsymbol{\psi}_i\}_{i=1}^{n_f}$ from $\{\boldsymbol{\chi}_i^e\}_{i=1}^{n_{\text{mpe}}}$.

Note that, in the remainder of this article, we refer to the set of coarse scale basis functions and fine-scale subdomain basis functions constructed from hierarchical finite element shape functions as the *hierarchical basis*. The set of coarse scale basis functions and fine scale subdomain basis functions constructed from empirical fine scale edge basis functions is referred to as *empirical basis*. In the latter case, we study two different training sets, namely the *structure of interest (Sol)* training set and the *random* training set, which are defined in section 3.1.4.

3.1.1 | Direct calculation of coarse scale basis functions

The coarse scale basis is required to form a partition of unity on the subdomain boundary $\partial\Omega_i$, to enable the assembly procedure to be described in section 3.2. Therefore, standard finite element shape functions on the boundary of the subdomain are extended into the interior by solving a variational problem on the RCE subdomain. The coarse scale basis functions are defined as the solution of

$$a(\boldsymbol{\varphi}_j, \mathbf{v}) = 0, \quad \boldsymbol{\varphi}_j = \boldsymbol{\Phi}_j \text{ on } \partial\Omega_i, \quad \forall \mathbf{v} \in \mathbb{V}_i, \quad (15)$$

where

$$a(\mathbf{w}, \mathbf{v}) = \sum_{m=1}^M \int_{\Omega_i^m} \lambda_m^1 \text{tr}(\boldsymbol{\varepsilon}(\mathbf{w})) \text{tr}(\boldsymbol{\varepsilon}(\mathbf{v})) + 2\lambda_m^2 \boldsymbol{\varepsilon}(\mathbf{w}) \cdot \boldsymbol{\varepsilon}(\mathbf{v}) \, dV \quad (16)$$

and $\boldsymbol{\Phi}_j$ being the standard Lagrange basis functions, which are constructed from Lagrange ploynomials (see⁴²)

$$l_k^q(\xi) = \frac{(\xi - \xi_0)(\xi - \xi_1) \cdots (\xi - \xi_{k-1})(\xi - \xi_{k+1}) \cdots (\xi - \xi_q)}{(\xi_k - \xi_0)(\xi_k - \xi_1) \cdots (\xi_k - \xi_{k-1})(\xi_k - \xi_{k+1}) \cdots (\xi_k - \xi_q)}, \quad (17)$$

giving unity at ξ_k and passing through q points. In two dimensions, the node j of the coarse grid element may be labeled by its column and row number, I, J ,

$$\boldsymbol{\Phi}_j = l_I^q(\xi) l_J^r(\eta). \quad (18)$$

The integer q and r stand for the number of subdivisions in each direction and ξ and η for the reference coordinates. For quadrilateral coarse grid cells in the two dimensional case and linear interpolation in the coarse scale, this yields a coarse scale basis of size $n_c = 8$, which is used in the remainder of the article.

3.1.2 | Calculation of fine scale edge basis functions

As mentioned in the beginning of section 3.1, two different approaches are considered. The fine scale edge basis functions may be defined as *hierarchical* shape functions a priori. In this case, no precomputation is required and one could directly compute the extension of the edge basis into the interior of the subdomain, as described in section 3.1.3. The construction of the *empirical* fine scale edge basis poses the main challenge in the proposed framework. In order to exploit fine scale solutions of the PDE eq. (1) on any subdomain Ω_i , we make use of the concept of oversampling¹³. First, the oversampling domain $\hat{\Omega}$ is defined, such that $\Omega_i \subsetneq \hat{\Omega} \subset \Omega_{\text{gl}}$. Furthermore, the distance between the boundary $\partial\Omega_i$ and $\Gamma_\mu := \partial\hat{\Omega} \setminus \partial\Omega_{\text{gl}}$ is greater than zero, i. e. $\text{dist}(\Gamma_\mu, \partial\Omega_i) \geq \rho > 0$ for some ρ . Depending on the configuration for a particular Ω_i , $\Gamma_N := \partial\hat{\Omega} \cap \Sigma_N$ or $\Gamma_D := \partial\hat{\Omega} \cap \Sigma_D$ may be not empty and Neumann or Dirichlet boundary conditions of the global problem need to be considered in the oversampling as well. In order to sufficiently incorporate Dirichlet and Neumann boundary conditions in the reduced basis functions, several oversampling problems have to be defined. We also refer to the different oversampling problems as “configurations” due to the possible change in topology and boundary conditions for each problem. The challenge in solving eq. (1) on $\hat{\Omega}$ lies in the definition of the boundary data on Γ_μ which is used to exploit possible solutions of the PDE on Ω_i . Taking, for example, parametric boundary conditions on Γ_μ , for a specific numerical discretization, the maximum size of the parameter space \mathbb{P} is the number of degrees of freedom on Γ_μ . Consider for example $\hat{\Omega}$ as a 3×3 block of RCEs, as shown in fig. 3. With the RCE type I, discretized with 11 vertices per edge, as shown in fig. 5a, this leads to 120 vertices on Γ_μ . For linear triangular elements, this would lead to a parameter space $\mathbb{P} = \mathbb{R}^{240}$, where a dense uniform sampling as usually done in standard greedy approaches (see²²) is infeasible. For this reason, Buhr and Smetana³⁷ suggest to solve eq. (1) on $\hat{\Omega}$ with random boundary conditions on Γ_μ (i. e., the associated transfer operator \mathbf{T} is approximated by random sampling). Note, that the transfer operator \mathbf{T} maps functions on the boundary Γ_μ to the solution of the PDE on the target subdomain Ω_i . In this work, we adopt “Algorithm 1: Adaptive Randomized Range Approximation”³⁷ and modify it to include the solution of a global reduced problem in the training data in addition to the random boundary conditions that are necessary to approximate the full range of the transfer operator. By doing so, the local reduced space contains information about the macroscopic displacement state and a refinement of the global coarse grid discretization is avoided.

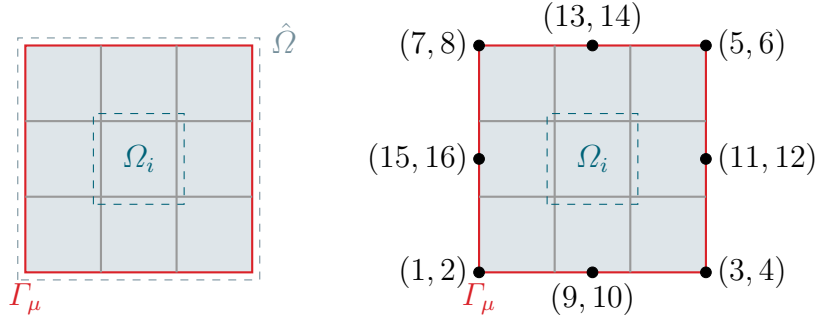


FIGURE 3 Oversampling domain $\hat{\Omega}$, target subdomain Ω_i , and the boundary Γ_μ for a target subdomain in the interior of the structure are shown on the left. The indices of the local degrees of freedom α_i are shown on the right.

We introduce shape functions Φ_i , which are chosen as standard finite element shape functions defined on the oversampling domain $\hat{\Omega}$, either of Lagrange or “serendipity” (see e. g. chapter 8 in⁴²) type. The number of degrees of freedom for the chosen shape functions is denoted as P . The function

$$g(\alpha^j) = \sum_{i=1}^P \Phi_i \alpha_i^j, \quad (19)$$

is introduced to describe the macroscopic displacement state of the chosen coarse grid element with cell index j . The coefficients $\alpha_i^j \in \mathbb{R}$ are the DoFs of the finite element with index j of the global reduced problem. As an example, fig. 3 shows the oversampling domain $\hat{\Omega}$ for a subdomain of interest Ω_i that is entirely inside the structure as well as the DoFs in the case of serendipity shape functions, with $P = 16$. A suitable training set is then defined as $S_{\text{train}} := \{g(\alpha^1), g(\alpha^2), \dots, g(\alpha^{n_\alpha}), g_r^1, g_r^2, \dots, g_r^{n_r}\}$, where g_r denotes random normal vectors on the boundary Γ_μ . The integer n_α and n_r refer to the number of physical and random training samples, respectively.

We use the term “random normal vector” in the same way as Buhr and Smetana³⁷, “to denote a vector whose entries are independent and identically distributed random variables with normal distribution.” We refer to section 3.1.4 for more details on the different training sets used in the numerical experiments and assume for now that a sufficient training set exists. The *oversampling problem*

$$\begin{aligned} -\nabla \cdot \sigma(\nabla \mathbf{u}) &= 0 && \text{in } \hat{\Omega}, \\ \sigma(\nabla \mathbf{u}) \cdot \mathbf{n} &= \hat{\mathbf{t}} && \text{on } \Gamma_N, \\ \mathbf{u} &= \mathbf{g}_D && \text{on } \Gamma_D, \\ \mathbf{u} &= \mathbf{g} && \text{on } \Gamma_\mu, \forall \mathbf{g} \in S_{\text{train}}, \end{aligned} \quad (20)$$

is then solved for \mathbf{u} for each element $\mathbf{g} \in S_{\text{train}}$ in the training set prescribed on the boundary Γ_μ .

The computation of the displacement snapshots is summarized in algorithm 1. Following Buhr and Smetana³⁷, we let \mathcal{P} be the probability, $P_{\text{span}(\mathbf{B})}$ the orthogonal projection onto $\text{span}(\mathbf{B})$, N_T the rank of the transfer operator \mathbf{T} and $\lambda_{\min}^{M_s}$ the smallest eigenvalue of the matrix of the inner product in the source space of the transfer operator. The “Algorithm 1: Adaptive Randomized Range Approximation”³⁷ is modified to simply return the unorthonormalized displacement snapshots, which then contain the same information as the orthonormalized basis \mathbf{B} . For constructing the fine scale edge basis, the solution of eq. (20) is restricted to the domain of interest, which is denoted by $\mathbf{u}|_{\Omega_i}$. This is equivalent to the image of the transfer operator of the boundary data ($\mathbf{u}|_{\Omega_i} = \mathbf{T}\mathbf{g}$). For each of the snapshots, the fine scale part is obtained by subtracting the coarse scale part and further restricted to the solution on the edges $\mathbf{u}_f|_{\Gamma_e^i}$. This way, four fine scale edge snapshots are obtained for each training sample and gathered in *snapshot sets* for edges opposite to each other, where a continuous coupling needs to be ensured. For example, a bottom-top-set and a right-left-set is defined for RCEs inside the structure. Finally, the edge snapshots are gathered column-wise in a so-called *snapshot matrix* and POD is then applied to compute the fine scale edge basis. It is noted that the POD algorithm⁴⁴ used in this paper computes the POD modes via the *method of snapshots*⁴⁵ which is summarized briefly in the paragraph below. The fine scale edge basis is denoted as $\{\chi_j^e\}_{j=1}^{n_{\text{mpe}}}$, with $e = 1, 2, 3, 4$ referring to one of the edges of the RCE domain Γ_e^i and n_{mpe} denoting the number of modes per edge. Note that for subdomains inside the structure, the sets $\{\chi_j^1\}_{j=1}^{n_{\text{mpe}}}$ (bottom) and $\{\chi_j^3\}_{j=1}^{n_{\text{mpe}}}$ (top) and analogously the sets $\{\chi_j^2\}_{j=1}^{n_{\text{mpe}}}$ (right) and $\{\chi_j^4\}_{j=1}^{n_{\text{mpe}}}$ (left) are identical.

Proper orthogonal decomposition

Given a set of N_{samples} snapshots $\{\mathbf{s}_i\}_{i=1}^{N_{\text{samples}}}$ the snapshot matrix $\mathbf{S} \in \mathbb{R}^{S \times N_{\text{samples}}}$ is defined as

$$\mathbf{S} = [\mathbf{s}_1, \mathbf{s}_2, \dots, \mathbf{s}_{N_{\text{samples}}}] . \quad (21)$$

In general, the snapshots can be vectors in a Hilbert space \mathbb{V} with dimension $S = \dim(\mathbb{V})$. Next, the correlation matrix $\mathbf{C} \in \mathbb{R}^{N_{\text{samples}} \times N_{\text{samples}}}$ is formed by the Gramian of the set of snapshots

$$C_{ij} = (\mathbf{s}_i, \mathbf{s}_j)_{\mathbb{V}}, \quad i, j = 1, 2, \dots, N_{\text{samples}} . \quad (22)$$

Then, the eigenvalue decomposition of the correlation matrix, with eigenvalues λ_k and eigenvectors \mathbf{v}_k , $k = 1, 2, \dots, \min(n_{\text{modes}}, N_{\text{samples}})$, is computed. Depending on the implementation, the number of POD modes n_{modes} can be specified directly by the user or in terms of a tolerance on the eigenvalues. The k -th POD mode χ_k is finally obtained by

$$\chi_k = \frac{1}{\sqrt{\lambda_k}} \mathbf{S} \mathbf{v}_k . \quad (23)$$

3.1.3 | Calculation of fine scale subdomain basis functions

The final step in constructing the reduced basis for the fine scale part of the displacement solution consists in the extension of the POD edge modes into the RCE domain Ω_i . It is important to note that, by setting the same function on a single edge for adjacent RCEs, continuity between adjacent subdomains is ensured. Furthermore, to enable the standard assembly procedure as in the finite element method, it is necessary to enforce zero boundary conditions on edges $\partial\Omega_i \setminus \Gamma_e^i$ where the POD mode is not prescribed. For each edge Γ_e^i , with $e = 1, 2, 3, 4$, and each POD mode in the set of edge basis functions $\{\chi_j^e\}_{j=1}^{n_{\text{mpe}}}$, find the subdomain basis function ψ_j^e such that

$$\begin{aligned} a(\psi_j^e, \mathbf{v}) &= 0, \quad \forall \mathbf{v} \in \mathbb{V}_i, \\ \text{with } \psi_j^e &= \chi_j^e \text{ on } \Gamma_e^i \quad \text{and} \quad \psi_j^e = \mathbf{0} \text{ on } \partial\Omega_i \setminus \Gamma_e^i, \end{aligned} \quad (24)$$

where the bilinear form $a(\cdot, \cdot)$ is given by eq. (16). All $n_f = 4n_{\text{mpe}}$ solutions of eq. (24) are then gathered in one set of fine scale basis functions

$$\{\psi_j\}_{j=1}^{n_f} = \{\psi_k^1\}_{k=1}^{n_{\text{mpe}}} \cup \{\psi_k^2\}_{k=1}^{n_{\text{mpe}}} \cup \{\psi_k^3\}_{k=1}^{n_{\text{mpe}}} \cup \{\psi_k^4\}_{k=1}^{n_{\text{mpe}}} . \quad (25)$$

3.1.4 | Training sets

In this section, two different choices for the training set which are studied in the numerical examples (section 4) are discussed.

The choice for the first training set is related to the particular choice of the coarse grid discretization, i. e. eq. (19), in the oversampling problem, in which it is assumed that the macroscopic response in most applications is well approximated by quadratic polynomials. Another motivation for this choice is the possibility to include physical states that are actually present in the *structure of interest* (*SoI*) and hence it is referred to as the *SoI* training set. To this end, prior to the solution of the oversampling problem, a reduced global problem is solved to obtain an approximation of the macroscopic deformation of the structure. There are several choices for the reduced global problem. For instance, the ROM using only the coarse scale basis can be used to obtain a displacement solution, which is used to inform the oversampling problem for the construction of the fine scale basis. In this line of thought, one may also employ an iterative strategy to construct the fine scale basis functions taking into account ROM solutions of different resolution. Another option is the solution of a standard FE problem on the coarse grid with homogenized material parameters. Note that in the absence of a clear scale separation, this gives inaccurate results and a homogenization should be avoided. However, in the present paper we are interested in an estimate of the macroscopic and for simplicity make use of this ansatz. The coefficients $\alpha_i \in \mathbb{R}$ are then given by DoFs local to each coarse grid cell, i. e. quadrilaterals with quadratic shape functions in this case. The training data $\{\mathbf{g}(\alpha^j)\}_{j=1}^{N_c}$ is compressed by a POD to avoid redundant information in the computation of the snapshots. The final *SoI* training set consists of the *SoI* POD modes and as many random normal vectors \mathbf{g}_r as needed to fulfill the target accuracy tolerance in the modified adaptive range finder algorithm (algorithm 1).

The second training set is referred to as *random* training set, because only random normal vectors \mathbf{g}_r are used in the solution of the oversampling problem eq. (20).

3.2 | Reduced order model

The proposed approach features a local basis $\{\xi_k\}_{k=1}^n = \{\varphi_i\}_{i=1}^{n_c} \cup \{\psi_j\}_{j=1}^{n_f}$, with n being the maximum number of basis functions, which constitutes a partition of unity for all vertices of the coarse grid and is continuous on subdomain boundaries Γ_e^i . Here φ_i and ψ_j are the n_c coarse scale and n_f fine scale functions, respectively. The reduced basis can be expressed in the standard finite element basis ϕ_j associated with the fine grid

$$\xi_k = \sum_{j=1}^{n_\delta} \mathbf{B}_{jk} \phi_j, \quad (26)$$

where the k -th column of the matrix $\mathbf{B} \in \mathbb{R}^{n_\delta \times n}$ holds the coefficients of the k -th basis function. The local contribution of a subdomain is then given by

$$\mathbf{A}_n = \mathbf{B}^T \mathbf{A}_\delta^{\text{loc}} \mathbf{B}, \quad \mathbf{f}_n = \mathbf{B}^T \mathbf{f}_\delta^{\text{loc}}, \quad (27)$$

where $\mathbf{A}_\delta^{\text{loc}} \in \mathbb{R}^{n_\delta \times n_\delta}$ and $\mathbf{f}_\delta^{\text{loc}} \in \mathbb{R}^{n_\delta}$ denote the stiffness matrix and external force vector, respectively, of a subdomain. Note that unless body forces are present, $\mathbf{f}_\delta^{\text{loc}}$ is zero in case $\Gamma_e^i \cap \Sigma_N = \emptyset$ or $\hat{\mathbf{t}} = \mathbf{0}$ which is the case for most subdomains. Due to the above-mentioned properties of the reduced basis functions, the local contributions $\mathbf{A}_n \in \mathbb{R}^{n \times n}$ and $\mathbf{f}_n \in \mathbb{R}^n$ can be sorted into global vectors following the usual assembly procedure of standard finite elements, where each node, edge and face (3D) is associated with a fixed number of degrees of freedom (DoFs). The global system of the *reduced order model* of size $N \ll N_\delta$ is then written as

$$\mathbf{A}_N \mathbf{u}_N = \mathbf{f}_N, \quad (28)$$

where $\mathbf{A}_N \in \mathbb{R}^{N \times N}$, $\mathbf{f}_N \in \mathbb{R}^N$ and N is the number of unknown DoFs in the reduced order model.

Algorithm 1 Modified Adaptive Randomized Range Approximation

```

1: function COMPUTESNAPSHOTS( $T, \text{tol}, n_t, \epsilon_{\text{algofail}}$ )
   Input: Operator  $T$ , target tolerance  $\text{tol}$ , number of testvectors  $n_t$ , maximum failure probability  $\epsilon_{\text{algofail}}$ , training set  $\mathcal{S}_{\text{train}}$ 
   Output: Set of snapshots  $U$  containing the same information as the space  $R^n = \text{span}(B)$  with property
    $\mathcal{P}(\|T - P_{R^n}T\| \leq \text{tol}) > (1 - \epsilon_{\text{algofail}})$ 
2:    $U \leftarrow \emptyset$  ▷ initialize snapshot set
3:    $B \leftarrow \emptyset$  ▷ initialize basis
4:    $M \leftarrow \{Tg_r^1, \dots, Tg_r^{n_t}\}$  ▷ initialize test vectors
5:    $\epsilon_{\text{testfail}} \leftarrow \epsilon_{\text{algofail}}/N_T$ 
6:    $c_{\text{est}} \leftarrow \left[ \sqrt{2\lambda_{\min}^{M_S}} \text{erf}^{-1} \left( \sqrt{\epsilon_{\text{testfail}}} \right) \right]^{-1}$  ▷ determine error estimator factor
7:   while  $(\max_{t \in M} \|t\|_R) \cdot c_{\text{est}} > \text{tol}$  do
8:      $g \leftarrow$  draw sample from training set  $\mathcal{S}_{\text{train}}$ 
9:      $u \leftarrow Tg$ 
10:     $U \leftarrow U \cup \{u\}$ 
11:     $B \leftarrow B \cup \{u\}$ 
12:     $B \leftarrow \text{orthonormalize}(B)$ 
13:     $M \leftarrow \{t - P_{\text{span}(B)}t \mid t \in M\}$  ▷ orthogonalize test vectors to  $\text{span}(B)$ 
14:   end while
15:   return  $U$ 
16: end function

```

4 | NUMERICAL EXPERIMENTS

In this section, the performance of the empirical bases, constructed from either the *Sol* or the *random* training set (section 3.1.4), is studied and compared to the hierarchical basis as a naïve choice for the approximation of the fine scale part. In section 4.1, a block example is implemented to confirm the assumption that only a single local reduced space is necessary if the fine scale structure is the same for each subdomain. Next, a beam under the state of pure bending is analyzed for a varying ratio of the elastic moduli as a measure for the heterogeneity, and the empirical basis' performance is shown to be superior to that of the hierarchical basis for ratios greater than one. The applicability of the method to more complex problems (containing a stress singularity in this case) is demonstrated by the example of an L-shaped panel in section 4.3. Finally, the effect of the *Sol* training set is investigated by studying the local projection error (section 4.4). To this end, we also introduce the *spectral basis* constructed using “Algorithm 1: Adaptive Randomized Range Approximation”³⁷. In addition, we discuss the difference in computational cost between the global approximation obtained by creating a partition of unity via the GFEM and the methodology proposed in section 3. To conclude the section, details on the basis construction and the computational time of the FOM as well as offline and online phase of the ROM are given in section 4.5.

If not stated otherwise, the material parameters listed in table 1 are used. Triangular elements with quadratic shape functions are used for the fine grid discretization of the RCE types used in the examples. Figure 4 shows the results of the mesh convergence analysis carried out. For different levels of refinement, eq. (3) is solved on the RCE domain with boundary data given by eq. (32), and the error relative to a reference solution computed on the finest mesh is measured in the energy norm. The mesh is regarded as converged if the relative error in the energy norm is below one percent which leads to the discretizations as shown in fig. 5. In

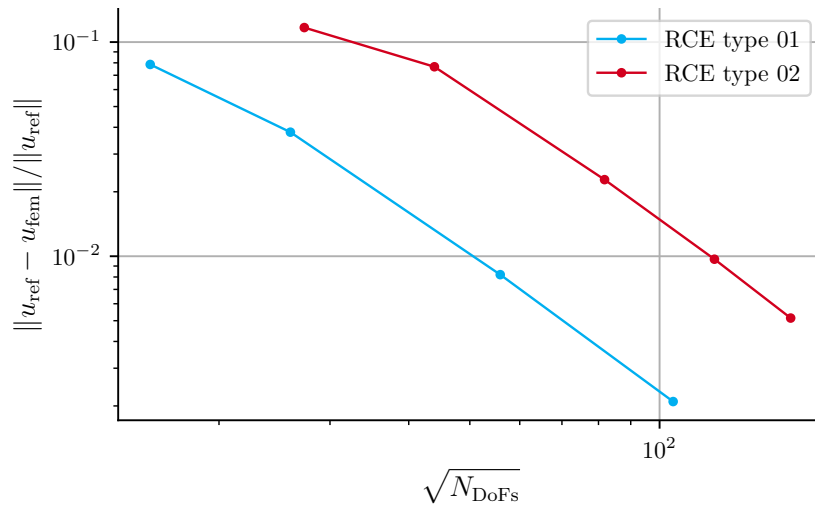


FIGURE 4 Relative error in the energy norm against square root of number of degrees of freedom in the mesh convergence analysis.

all examples, the global error relative to the *full order model* (eq. (3)) is computed as follows. The absolute error on subdomain Ω_i defined as $e_i = (u_{\text{fom}})_i - (u_{\text{rom}})_i$ is measured in the energy norm as

$$\|e_i\|_{V_i}^2 = a(e_i, e_i). \quad (29)$$

The global absolute error is thus given by the square root of the sum of the squared local norm

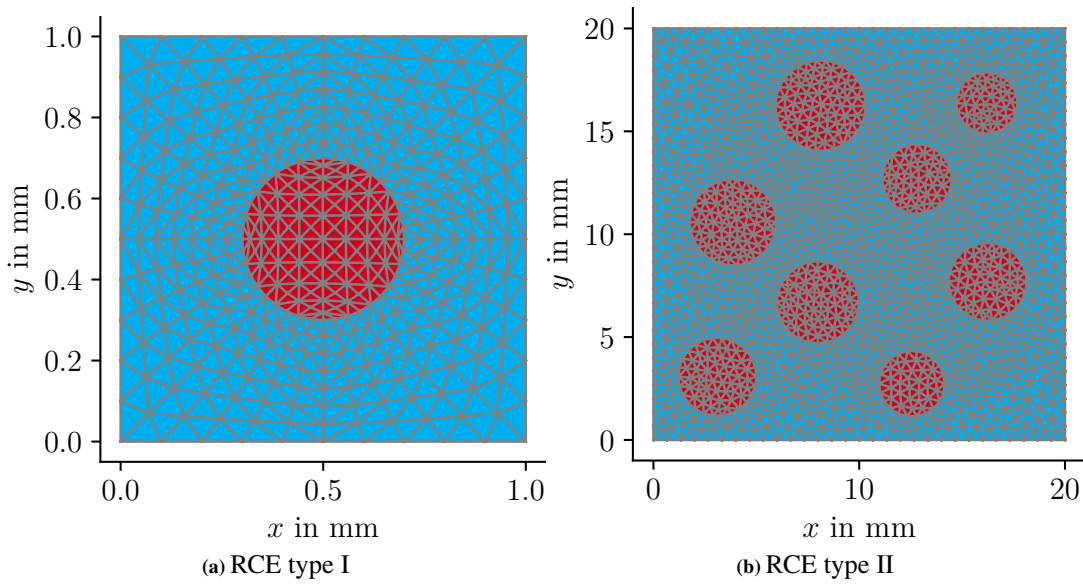
$$\|e\|_V = \sqrt{\sum_{i=1}^{N_c} \|e_i\|_{V_i}^2}. \quad (30)$$

TABLE 1 Material parameters (taken from table 4 in⁴⁶).

	Mortar matrix	Aggregates
Young's modulus	$E_m = 30\,000 \text{ MPa}$	$E_a = 60\,000 \text{ MPa}$
Poisson ratio	$\nu_m = 0.2$	$\nu_a = 0.2$

Analogously, the global relative error is given by

$$\frac{\|e\|_{\mathbb{V}}}{\|u_{\text{fom}}\|_{\mathbb{V}}} = \frac{\sqrt{\sum_{i=1}^{N_c} \|e_i\|_{\mathbb{V}_i}^2}}{\sqrt{\sum_{i=1}^{N_c} \|(u_{\text{fom}})_i\|_{\mathbb{V}_i}^2}}. \quad (31)$$

**FIGURE 5** RCE types used in the examples.

4.1 | Block example

In this example, eq. (1) is solved on a global domain $\Omega_{\text{gl}} = (0, 5)^2$ with Dirichlet data on the boundary $\Sigma_D := \partial\Omega_{\text{gl}}$ given in index notation by

$$u_i^D = a_{ij}x_j + b_{ij}x_j^2, \quad a_{ij}, b_{ij} \in \mathbb{R}. \quad (32)$$

An RCE of type one (fig. 5a) is used and, consequently, the coarse grid is chosen as a structured grid with five cells in each spatial direction. While the performance of the empirical basis using the *SoI* training set is compared to the empirical basis using the *random* training set, the discretization level of the RCE is controlled via the number of vertices per edge n_{verts} . Only a single oversampling problem with $\Gamma_\mu := \partial\hat{\Omega}$ is considered for the construction of the empirical basis for the respective training set. There is thus the assumption that, in this particular problem, the deformation of any RCE can be well approximated by a single set of empirical basis functions. Note that the additional training due to Dirichlet boundary conditions is not necessary since u_i^D lies in the span of the empirical basis $\{\xi_i\}_{i=1}^n$. The boundary conditions can be applied in the usual way by computing the corresponding values via projection of the Dirichlet data onto the empirical edge basis.

The global relative error with respect to the full order model is shown in fig. 6. The legend entries refer to the respective training set and discretization level, where *random* refers to the *random* training set and *SoI* refers to the *SoI* training set (see section 3.1.4).

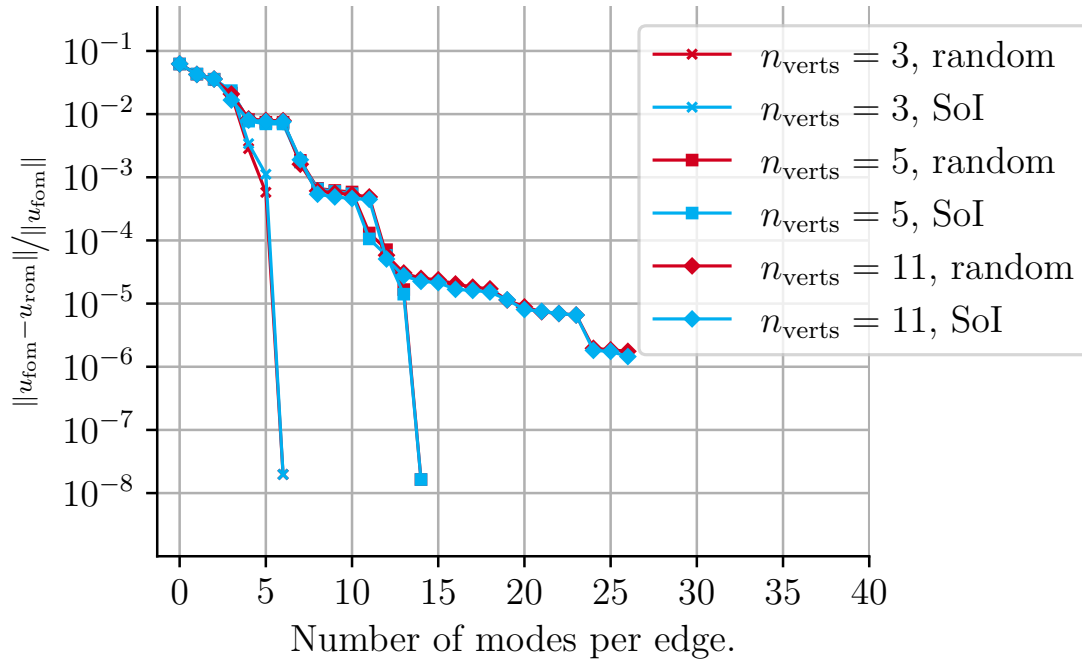


FIGURE 6 Block example: relative error in energy norm.

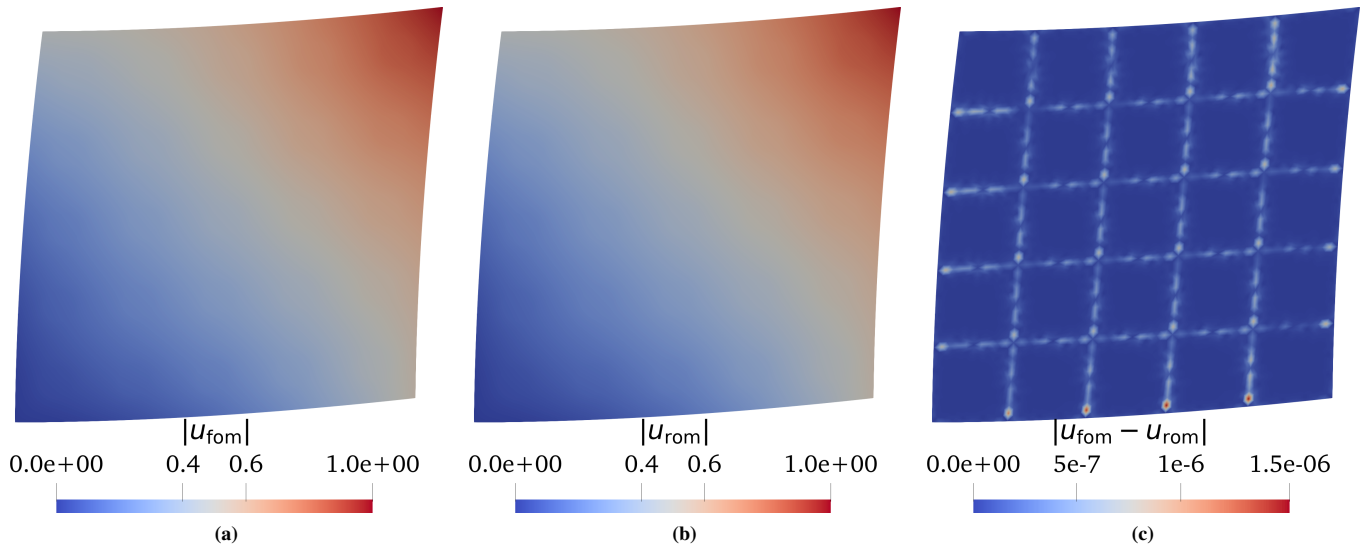


FIGURE 7 (a) Magnitude of FOM solution, (b) Magnitude of the ROM solution using the empirical basis with 15 modes per edge and (c) ROM error using the empirical basis with 15 modes per edge in the deformed placement. In all cases, a scale factor of 1 is used for the deformation. In case of the absolute error, the domain is scaled by the ROM solution.

In both cases, the discretization of the RCE has no effect on the quality of the reduced order model relative to the FOM. Also, in this example, both training sets yield a basis with equally good approximation capabilities. However, the maximum number of basis functions per edge is limited by the discretization, as can be observed for $n_{\text{verts}} = 3$ and $n_{\text{verts}} = 5$.

Furthermore, fig. 7 gives an impression of the solution and where the maximum error is located. In case of the empirical basis (fig. 7c), the maximum error is located at the boundary and edges perpendicular to the boundary, but for all interior edges roughly the same approximation error well below the prescribed target accuracy is obtained.

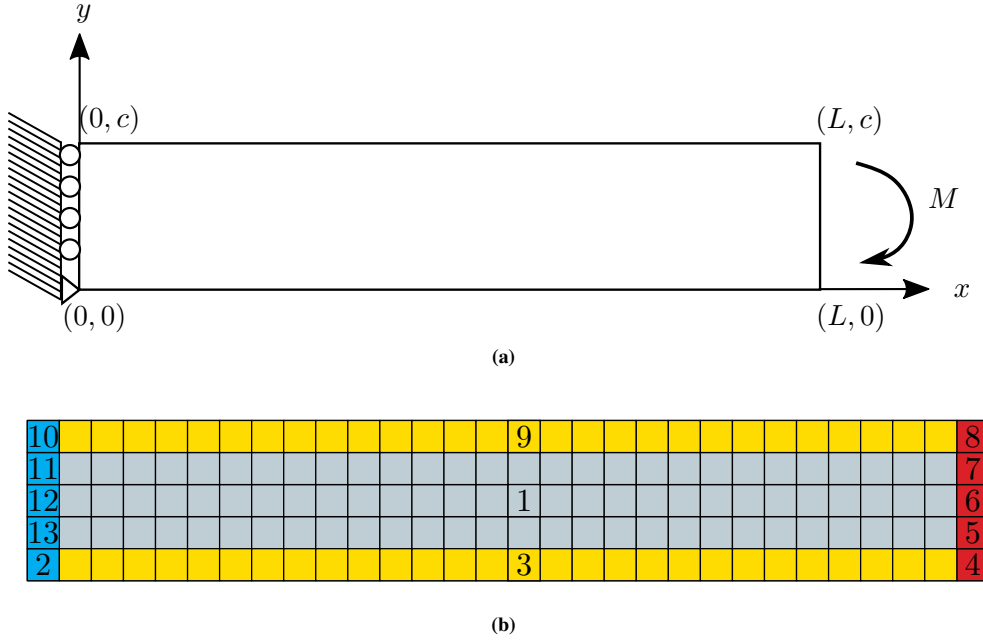


FIGURE 8 Schematic representation (a) of the beam problem and coarse grid discretization showing configurations to be considered in the offline phase (b).

4.2 | Beam example

A beam under the state of pure bending is considered on the domain $\Omega_{\text{gl}} = (0, L) \times (0, c)$ as illustrated in fig. 8a. The bending moment $M = 20c^2$ is distributed as $f_x = \frac{240y}{c} - 120$, such that the analytical solution (see⁴⁷) in the case of a homogeneous isotropic and linear elastic material is

$$\sigma_{xx} = \frac{240y}{c} - 120, \quad \sigma_{yy} = \tau_{xy} = 0, \quad (33)$$

$$u = \left(\frac{240}{c}xy - 120x \right) \frac{1}{E}, \quad (34)$$

$$v = -\frac{\nu}{E} \left(\frac{120}{c}y^2 - 120y \right) - \frac{1}{E} \frac{120}{c}x^2. \quad (35)$$

In this example, the empirical basis (using the *SoI* as well as *random* training set) is compared to the hierarchical basis for varying ratio E_a/E_m of Young's moduli of the aggregates and matrix.

The dimensions of the beam L and c are chosen such that the coarse grid consists of 50×50 RCEs of type II, see fig. 5b. Therefore, in total, 13 oversampling problems which take into account the Dirichlet and Neumann boundary conditions are considered in the offline phase (see fig. 8b). The blue configurations take into account the homogeneous Dirichlet boundary conditions. The inhomogeneous Neumann boundary conditions are taken into account by the red configurations. In analogy to the block example (section 4.1), all interior subdomains are approximated by the same set of basis functions (gray configurations). Finally, in case of target subdomains whose boundaries $\partial\Omega_i$ intersect with the boundary of the global domain $\partial\Omega_{\text{gl}}$, one configuration (marked with yellow color) is considered for each Neumann boundary.

To illustrate the change in topology, the oversampling domain $\hat{\Omega}_2, \hat{\Omega}_{13}, \hat{\Omega}_{12}, \hat{\Omega}_{11}$ and $\hat{\Omega}_{10}$, with their respective target subdomain $\Omega_2, \Omega_{13}, \Omega_{12}, \Omega_{11}$ and Ω_{10} are shown in fig. 9.

As a consequence of the chosen configurations in the offline phase, in case of the empirical basis there is no need to prescribe fine scale boundary conditions. Here, we only set the appropriate DoF values associated with the coarse scale basis functions. In case of the *hierarchical basis*, for the coarse scale basis functions we proceed in the same manner and compute the boundary values to be prescribed for the fine scale functions via projection.

For varying ratio E_a/E_m of Young's moduli for the aggregates and matrix, the global relative error is shown in fig. 10. In the homogeneous case, i.e. $E_a/E_m = 1$, for the hierarchical basis it amounts to a nested finite element method and for the number

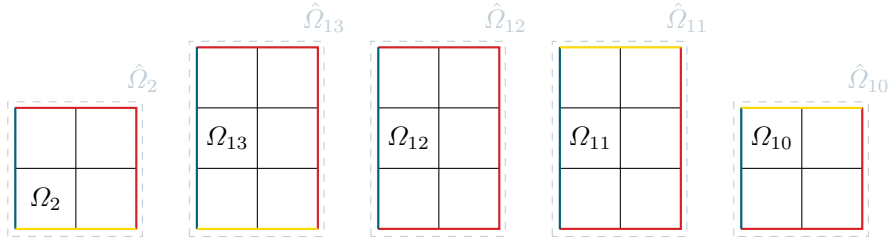


FIGURE 9 The configurations of the oversampling domain $\hat{\Omega}$ for the subdomains $\Omega_2, \Omega_{13}, \Omega_{12}, \Omega_{11}, \Omega_{10}$ on the left Dirichlet boundary in case of the beam example. The colors indicate the boundaries Σ_D (blue), Σ_N (yellow) and Γ_μ (red) whose topology is changing.

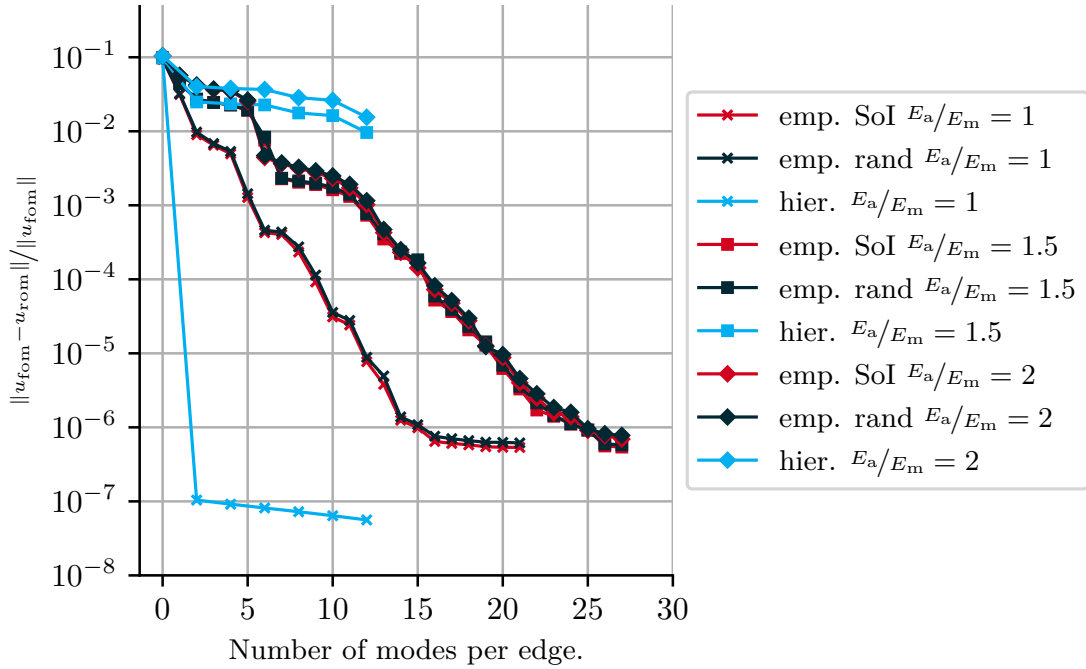


FIGURE 10 Beam example: relative error in the energy norm against number of modes per edge. The empirical basis (*SoI* and *random* training set) and hierarchical basis are compared for varying ratio of Young's moduli.

of modes per edge $n_{\text{mpe}} \geq 2$ the analytical solution can be exactly represented. However, for ratios $E_a/E_m > 1$, the hierarchical basis does not yield a good approximation of the fine scale part of the displacement, whereas the relative error is already below $1 \cdot 10^{-3}$ for the empirical bases using 12 modes per edge.

Moreover, in case of the empirical bases, the error in the local approximation does carry over to the global approximation. As a rule of thumb, assuming the same local error norm for each subdomain $\|e_i\|_{V_i} := \text{tol}$, i. e. assuming the same target accuracy for each local space was reached, one can expect a global error norm $\|e\|_V = \sqrt{N_c} \text{tol}$. Consequently, depending on the target accuracy prescribed in the offline phase, the global error stagnates when falling below this limit, which explains the stagnation of the global relative error in case of the empirical bases for ratio $E_a/E_m = 1.5$. This can be improved by choosing a smaller target tolerance for each of the oversampling problems or ideally a strategy can be developed in which the target tolerance for each oversampling problem is chosen in order to reach a certain global error. The latter was already demonstrated by Buhr and Smetana³⁷ when using the GFEM to build a global approximation.

The displacement solution of the different models and the absolute error in the displacements are shown in fig. 11.

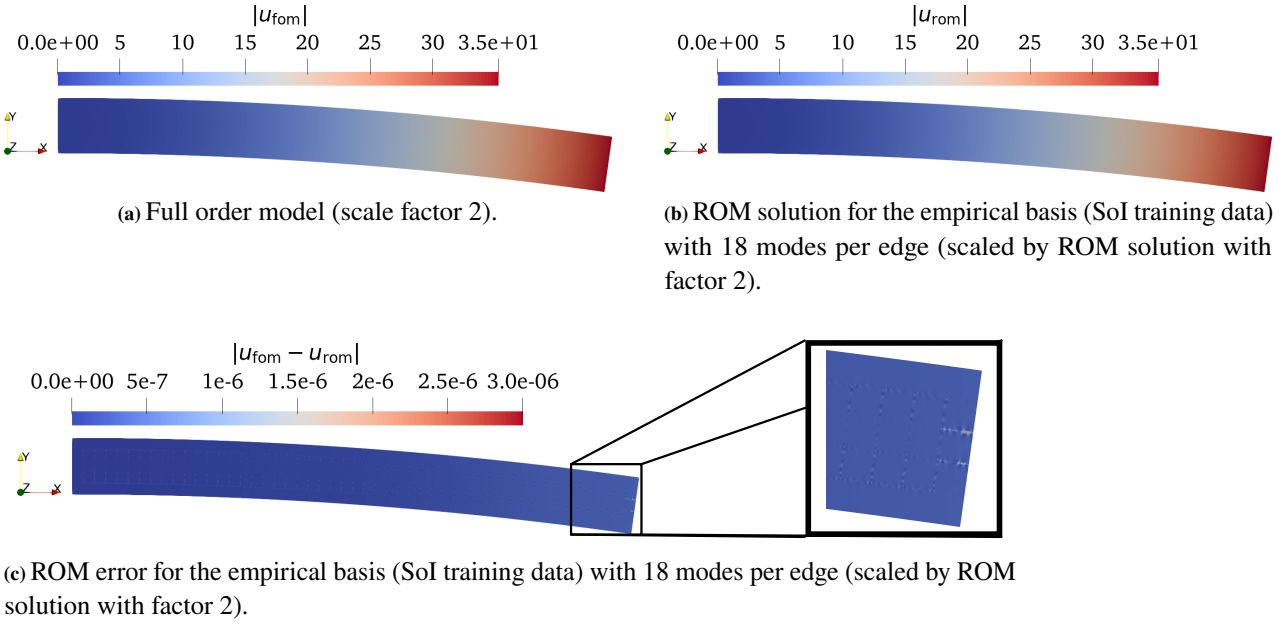


FIGURE 11 Magnitude of the displacement solution for (a) the FOM (b) the ROM and (c) the absolute error in the deformed placement for ratio of Young's moduli $E_a/E_m = 2$.

4.3 | L-panel example

The third example is an L-shaped panel, see fig. 12a. It features a more complex geometry and a concentrated load modeled as a Neumann boundary condition. For simplicity, the load is modeled as a linearly varying hat function with maximum value $t_y = 200 \text{ N/mm}^2$ distributed over two coarse grid cells, such that the maximum vertical displacement is $u_y \approx 5.4 \text{ mm}$. Again RCE type II (see fig. 5b) is used leading to the coarse grid and configurations as shown in fig. 12b. The different configurations are encoded by color in the same manner as in the beam example (section 4.2). In case of the L-Panel, the *random* training set is compared to the *SoI* training set for the *empirical basis* in terms of the global relative error with regard to the FOM.

There is almost no difference between the two training sets in terms of the resulting global relative error with respect to the FOM solution (see fig. 13). This is mainly due to the fact that the *SoI* training set contains all local solutions for the entire structure. Since the deformation states of the RCEs vary greatly over the whole structure, the local spaces are not specifically tailored to the state dominant in a certain area of the structure. Moreover, fig. 14 shows the absolute error between the FOM and the ROM for the L-panel. In agreement with the other examples, the same level of accuracy is achieved for the entire domain, while the largest errors are located at subdomain interfaces. In addition, near the recessed corner, which is known to be the critical area of the structure, the error level seems to be slightly larger. Nonetheless, the displacement field in this area is well approximated.

4.4 | Projection error study

The purpose of this section is on the one hand to compare how the *SoI* training set and the *random* training set defined in section 3.1.4 influence the decay of the maximum local relative projection error, i. e. the local approximation capabilities of the reduced bases. On the other hand, the maximum local relative projection error is investigated with regard to the local number of basis functions and the actual computational cost one could expect in the online phase. To this end, the oversampling problem eq. (20) is solved with $\partial\hat{\Omega} = \Gamma_\mu$ to construct in total four different sets of basis functions. As outlined in section 3, empirical bases are constructed using (a) the *SoI* training set and (b) the *random* training set. Moreover, *spectral bases* are constructed using “Algorithm 1: Adaptive Randomized Range Approximation” in Buhr & Smetana³⁷ with (a) the *SoI* training set and (b) the *random* training set. We note that, the empirical basis is constructed by solving the oversampling problem and extracting only the fine scale edge snapshots, which are then compressed via POD and subsequently extended into the RCE domain, whereas the spectral basis is directly computed by restricting the solution of the oversampling problem to the RCE domain. Therefore, one has to consider that a single spectral basis function may be equivalent to (in the 2d case) $n_c = 8$ coarse

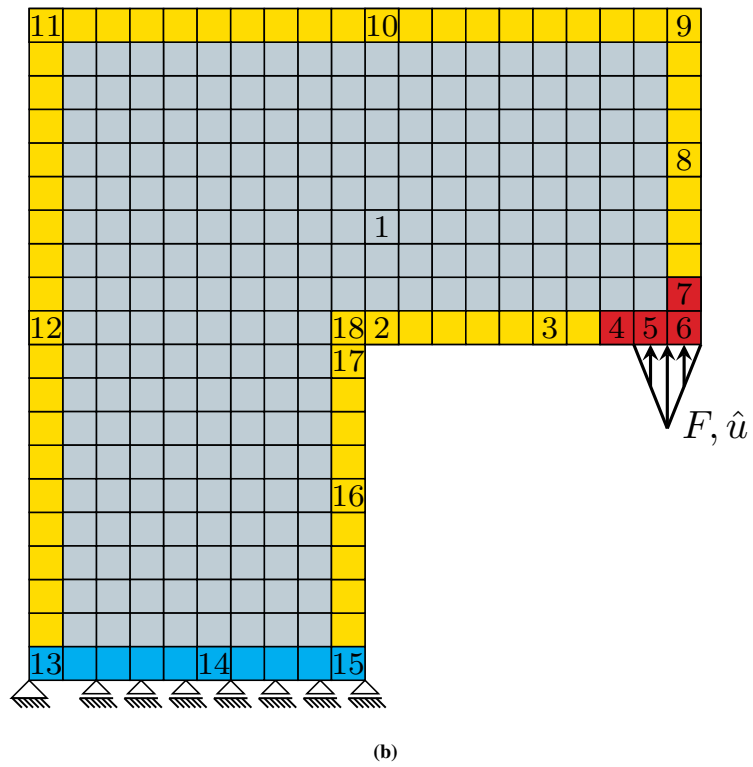
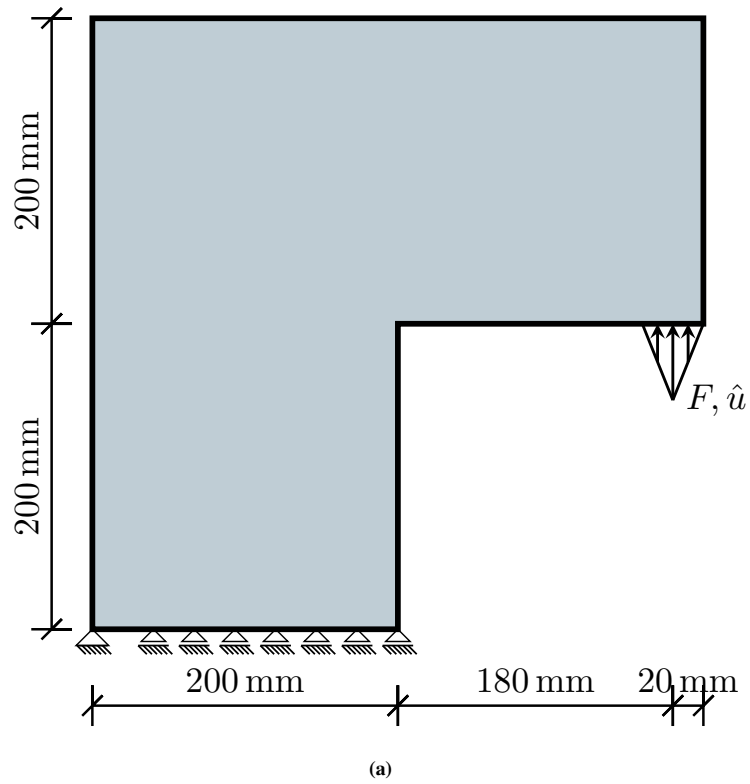


FIGURE 12 Schematic representation (a) and different configurations present in the chosen coarse grid (b) of the L-Panel example.

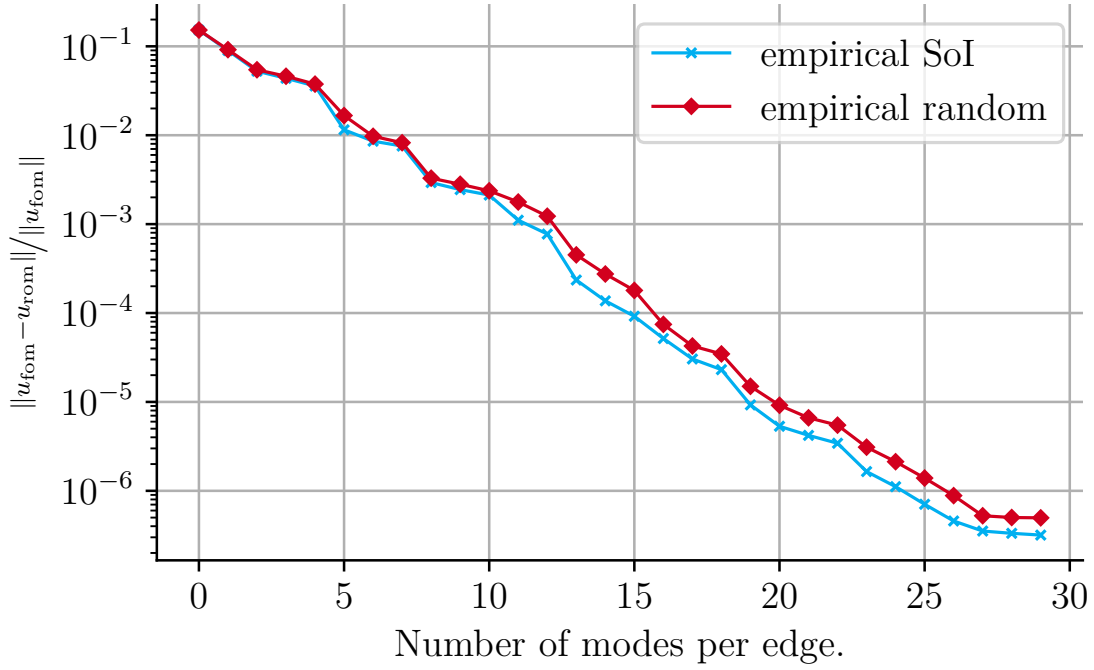


FIGURE 13 L-Panel example: global relative error in the energy norm against number of modes per edge.

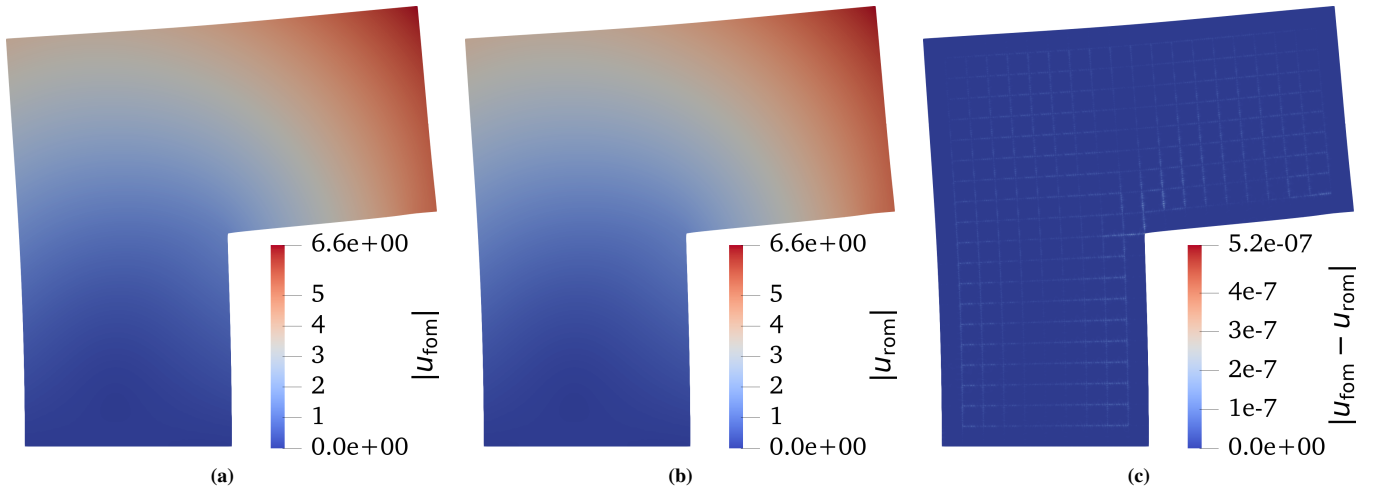


FIGURE 14 Magnitude of the displacement solution for FOM (a) and ROM (b), both with a scale factor of 5. The ROM error (c) is shown in case of the empirical basis (*SoI* training set) using 20 modes per edge.

scale functions φ_i and four fine scale subdomain functions ψ_j . The spectral basis functions are non-zero on the boundary of the RCE domain $\partial\Omega_i$, while the empirical fine scale subdomain basis functions are only non-zero for one of the edges Γ_e^i of $\partial\Omega_i$. For the *SoI* training set, the data of the L-Panel example (section 4.3) is considered and therefore the RCE type II (fig. 5b) is used.

All four bases are tested against a random testing set (with a different random seed than the training set) and a testing set constructed from the FOM solution of the L-Panel example. The *random testing set* of size n_{test} comprises the solutions of the oversampling problem restricted to the target subdomain Ω_i , for n_{test} random vectors prescribed on the boundary Γ_μ . The *FOM testing set* consists of the FOM solution restricted to the RCEs in the interior of the structure. For the chosen coarse grid discretization, this results in $n_{\text{test}} = 224$ RCE solutions (cells coloured in gray in fig. 12).

The maximum local relative projection error for a given testing set $\{s_1, s_2, \dots, s_{n_{\text{test}}}\}$ with n_{test} test vectors and a basis $\{\eta_k\}_{k=1}^n$ is given as

$$\max_j \frac{\left\| s_j - \sum_{k=1}^n (s_j, \eta_k)_{V_i} \eta_k \right\|_{V_i}}{\left\| s_j \right\|_{V_i}}. \quad (36)$$

Again, we choose the energy norm to measure the error and note that, in case of the empirical basis, which is not orthonormal with respect to the energy inner product the projection coefficients $(s_j, \eta_k)_{V_i}$ have to be computed by solving a linear system of equations. The variants of the spectral basis are orthonormalized with respect to the energy inner product.

Next, we discuss how a global approximation can be obtained for the empirical or the spectral basis and how many DoFs in the global approximation one could expect. We note that due to the decomposition of the fine scale part into several functions which are non-zero for only one edge of the RCE boundary, the number of local empirical basis functions is greater than the number of local spectral basis functions. However, this decomposition avoids an overlap of the target subdomains in the oversampling, which is, to the authors' knowledge, necessary when generating a partition of unity by use of the GFEM. Thus, in addition to computing the projection error as a function of the number of basis functions which is only one measure of the quality, but does not characterize the performance in the global approximation, the projection error is also compared to the total number of DoFs in the global approximation. To this end, we consider the discretizations of the unit square as shown in fig. 16. In case of the empirical basis, the objective is to construct local spaces on target subdomains Ω_i which have dimension $1/3$ in width and height (i. e. coarse grid parameter $h = 1/3$) on the global domain $\Omega_{\text{gl}} = (0, 1)^2$. The total number of DoFs in the global approximation is then given by the number of vertices n_v in the coarse grid multiplied by the number of coarse scale basis functions n_c plus the number of edges n_e in the coarse grid multiplied by the number of fine scale edge modes n_{mpe} .

$$N_{\text{dofs}}^{\text{emp}} = n_v n_c + n_e n_{\text{mpe}}. \quad (37)$$

For the given example we have $n_v = 4^2$ vertices and $n_e = 24$ edges.

Regarding the spectral basis, a global approximation can be obtained by the GFEM. In particular, we refer to the procedure outlined in example 4.4 of³⁷. Due to the overlap of the target subdomains required to construct a global approximation via the GFEM, a smaller coarse grid resolution (here $h = 1/6$ for an overlap of size $1/6$) is needed. The total number of DoFs is given by the number of vertices n_v in the coarse grid multiplied by the local number of basis functions n .

$$N_{\text{dofs}}^{\text{spe}} = n_v n. \quad (38)$$

Due to the smaller coarse grid resolution, in this case we have $n_v = 7^2$ vertices.

Finally, the decay of the local relative projection error is plotted against the local number of basis functions n and the number of DoFs in the resulting global approximation in fig. 15 and fig. 17 for the respective testing sets. In case of the empirical basis, the error is (empirically) shown to decay exponentially for both testing sets. Figure 15 also shows the positive effect of the *SoI* training data on the projection error decay regarding the spectral basis. As explained above, the decomposition of the fine scale part in the empirical basis functions, leads to a less rapid decay of the projection error as a function of the number of local basis functions. However, the proposed empirical basis is shown to yield global approximations with much fewer DoFs than the spectral basis (in combination with the GFEM) in the numerical model while achieving the same level of accuracy.

4.5 | Basis construction and computational time

All simulations, comprising FOM and ROM (offline as well as online), are carried out using a single core (Intel Core i7-10700) and serial implementations. It is noted that the current implementation is not optimized and the provided numbers regarding computation time serve as a proof of concept rather than a rigorous comparison of the computational performance of both models.

Regarding the offline phase, in each of the oversampling problems of all examples, a target tolerance $\text{tol} = 1 \cdot 10^{-3}$, a failure tolerance $\epsilon_{\text{algofail}} = 1 \cdot 10^{-15}$, and $n_t = 20$ test vectors were used. Furthermore, for the norm induced by the source and range space of the transfer operator, the L^2 and energy inner products were used, respectively. With regard to the POD compression, the edge space was equipped with the L^2 inner product and a relative tolerance of $1 \cdot 10^{-6}$ was set.

A comparison of the total number of DoFs in the numerical models is given in table 2. For each of the investigated examples, the computational time needed to solve the FOM and ROM are given in table 3. Regarding the time needed to construct the empirical basis, the minimum, maximum and average time over all oversampling problems is reported. To estimate the total computational time to evaluate the ROM, it is noted that the construction of the local reduced spaces is easily parallelizable since

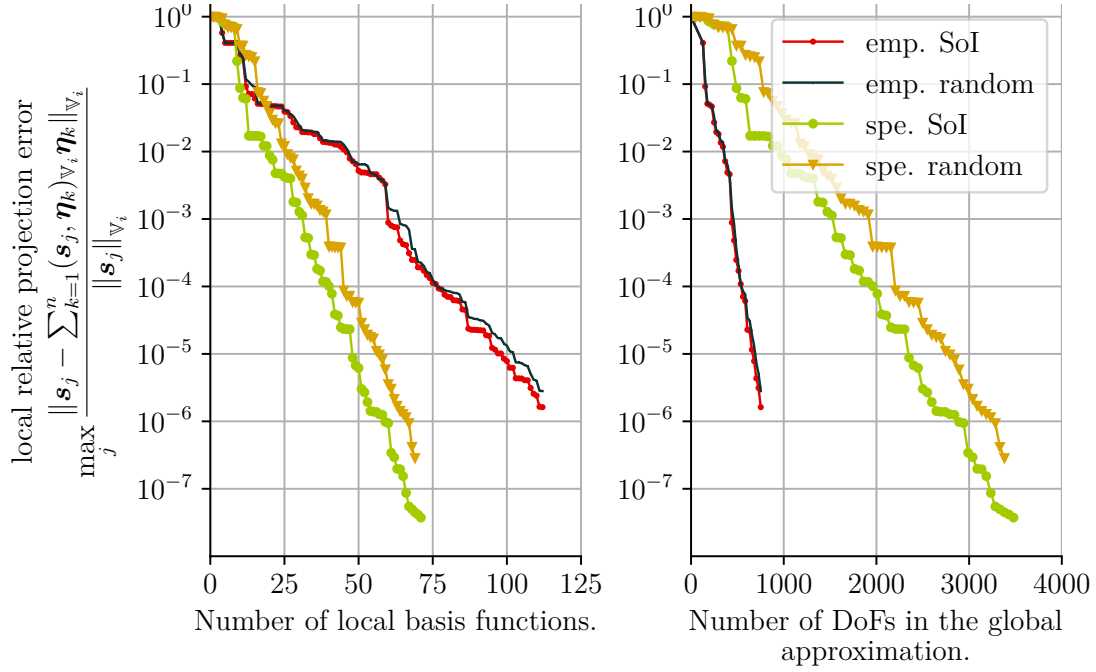


FIGURE 15 Local relative projection error with respect to the L-Panel testing set (FOM solution excluding coarse grid elements in the boundary layer) of size 224. On the left, the projection error is plotted against the number of local basis functions, whereas on the right it is plotted against the total number of DoFs in the global approximation of the block example shown in fig. 16. The legend labels refer to the basis type and training set.

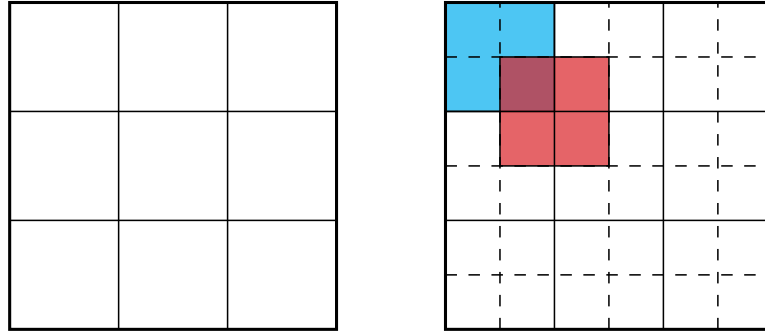


FIGURE 16 Coarse grid discretizations of the unit square. The coarse grid with mesh parameter $h = 1/3$ to be used in conjunction with the empirical basis is shown on the left. On the right, the overlap of the target subdomains in the construction of the local spaces, necessary for the global approximation via the GFEM, and the resulting coarse grid resolution with $h = 1/6$ is shown.

there is no dependency or need to communicate between the different oversampling problems. Hence, the total time consists of the time needed to construct the local basis for the computationally most expensive oversampling problem and time of the online phase. The computational time for the online phase of the ROM (using 20 modes per edge) and the FOM comprise the time needed to assemble and solve the system of equations. The ROM is evaluated ≈ 1.5 times faster than the FOM in case of the beam and L-panel example. We also note that - given the computational time needed to solve the FOM - the investigated examples are rather toy problems and that the comparison will be more in favor of the ROM for larger problems.

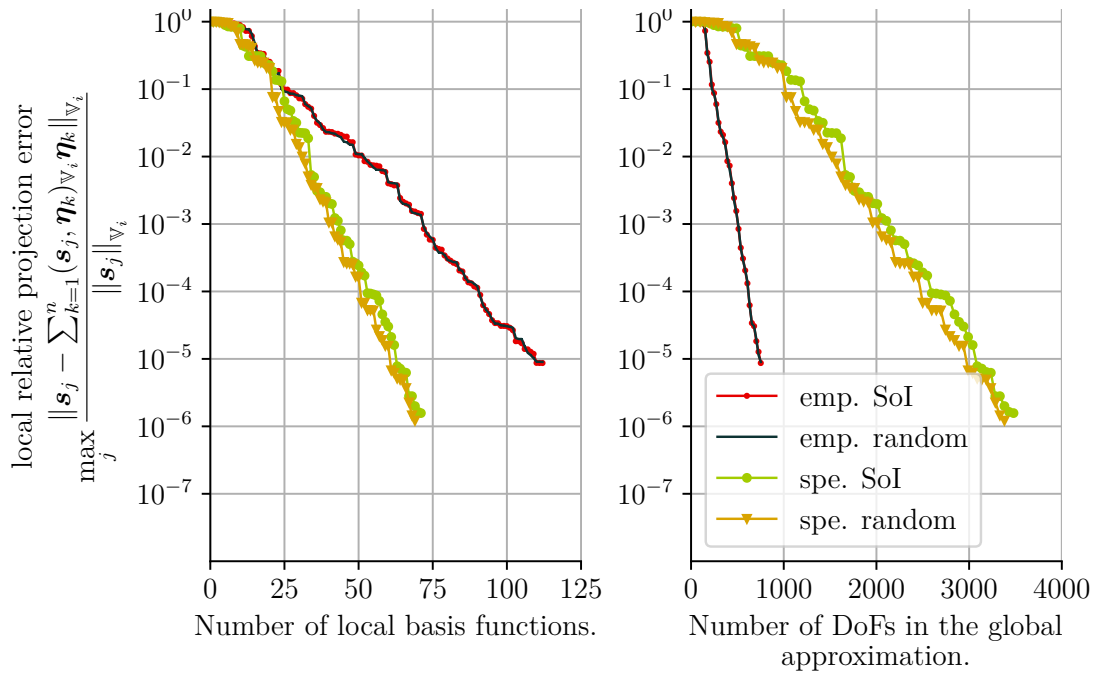


FIGURE 17 Local relative projection error with respect to the random testing set of size 200. On the left the projection error is plotted against the number of local basis functions, whereas on the right it is plotted against the total number of DoFs in the global approximation of the block example shown in fig. 16. The legend labels refer to the basis type and training set.

TABLE 2 Total number of DoFs of FOM and ROM for the example problems.

Example problem	FOM	ROM (20 modes per edge)
Block	76402	1272
Beam	3678602	11015
L-Panel	4411202	12960

TABLE 3 Computational time in seconds.

Example problem	ROM (20 modes per edge)					FOM	
	offline			online			
	min	max	avg	assembly	solve	assembly	solve
Block	0.06	8.51	6.22	0.09	0.03	0.11	0.35
Beam	6.63	23.41	11.27	0.29	0.83	13.69	22.26
Lpanel	7.79	23.24	13.08	0.23	2.39	14.86	24.94

5 | CONCLUSIONS

In this contribution, a methodology to model linear elastic heterogeneous structures is presented. A method combining the variational multiscale method, domain decomposition and model order reduction techniques is developed and applied to model the influence of the fine scale on the coarse scale directly. Herein, snapshots of the displacement field for local target subdomains are computed by solving an oversampling problem with physically informed — by solving a global reduced problem — as well as random boundary conditions. Based on the displacement snapshots, a fine scale edge basis is constructed via POD and a

conforming approximation is obtained by extending the edge functions into the interior of the respective subdomain. This then allows for a conforming coupling of the reduced coarse grid elements in the framework of standard finite element assembly and hence an easy implementation. The resulting global system of equations is sparse and reduced in size compared to the full order model.

The physically informed boundary conditions in the oversampling problem are shown to improve the approximation capabilities of the reduced local spaces. However, the decomposition of the fine scale part into edge functions and subsequent extension into the interior of the subdomains seems to mitigate this positive effect. Moreover, currently only a single local subdomain space for the interior is constructed using the same training set and the same space is used throughout the interior of the entire structure. Possibly for a more efficient reduction and positive effect of the physically informed boundary conditions, one would like to group the training data by means of clustering methods and analogously construct several local spaces, each tailored specifically to the displacement state of the respective cluster, for the interior of the structure.

Nevertheless, means to include physical states and their variation in the training data is promising in view of the extension of the method to the nonlinear case, which is subject of future work. In contrast to the linear case, the choice of the correct amplitudes of the boundary data in the oversampling problem or amplitudes of the edge modes when extending these into the respective subdomain poses a great challenge. Moreover, regarding the hyper-reduction methods referred to in section 1, usually a second projection subspace for the nonlinear term is needed. The choice of the snapshots for the second subspace — in the context of solid mechanics this is a subspace for the stresses — is not trivial and several approaches exist in the literature. Examples are the use of non-equilibrated snapshots of the Newton iteration⁴⁸ or the use of statically inadmissible stress approximations in addition to the equilibrated snapshots⁷.

For an efficient reduction of nonlinear problems, an adaptive solution procedure is necessary due to the growing size of the local spaces and an optimal use of available resources. However, for fully localized problems, a reduction might be very challenging, such that a hybrid approach in which one can switch back to a FOM for certain subdomains depending on the deformation state is envisioned. To this end, the fine scale information contained in the reduced basis functions is needed to develop criteria for the transition from a ROM to a FOM which is possible with the proposed framework and planned as future work.

ACKNOWLEDGEMENTS

The authors gratefully acknowledge financial support by the German Research Foundation (DFG), project number 394350870, and by the European Research Council (ERC) under the European Union's Horizon 2020 research and innovation programme (ERC Grant agreement No. 818473).

CODE AVAILABILITY

The complete workflow, i. e. all tasks to process and postprocess the numerical experiments described in this article, are implemented using the automation tool *doit*⁴⁹. The source code necessary to *reproduce* the results is published together with the open source preprint⁵⁰ of this article and publicly available. The numerical experiments are implemented with a self-written code based on the open source computing platform FEniCS⁵¹.

References

1. Miehe C, Koch A. Computational micro-to-macro transitions of discretized microstructures undergoing small strains. *Archive of Applied Mechanics (Ingenieur Archiv)* 2002; 72(4-5): 300-317. doi: 10.1007/s00419-002-0212-2
2. Feyel F, Chaboche JL. FE2 multiscale approach for modelling the elastoviscoplastic behaviour of long fibre SiC/Ti composite materials. *Comput. Method. Appl. M.* 2000; 183(3-4): 309-330. doi: 10.1016/s0045-7825(99)00224-8
3. Geers M, Kouznetsova V, Brekelmans W. Computational homogenization. In: Pippan R, Gumbsch P., eds. *Multiscale Modelling of Plasticity and Fracture by Means of Dislocation Mechanics* Vienna: Springer Vienna. 2010 (pp. 327-394)

4. Geers M, Kouznetsova V, Brekelmans W. Multi-scale computational homogenization: Trends and challenges. *J. Comput. Appl. Math.* 2010; 234(7): 2175-2182. doi: 10.1016/j.cam.2009.08.077
5. Yvonnet J, He QC. The reduced model multiscale method (R3M) for the non-linear homogenization of hyperelastic media at finite strains. *J. Comput. Phys.* 2007; 223(1): 341-368. doi: 10.1016/j.jcp.2006.09.019
6. Goury O, Kerfriden P, Bordas S. Bridging analytical and computational homogenisation for nonlinear multiscale problems: A reduced order modelling approach for a damage problem. tech. rep., Cardiff University, School of Engineering; Cardiff, UK: 2014.
7. Hernández J, Oliver J, Huespe A, Caicedo M, Cante J. High-performance model reduction techniques in computational multiscale homogenization. *Comput. Method. Appl. M.* 2014; 276: 149-189. doi: 10.1016/j.cma.2014.03.011
8. Guo T, Rokoš O, Veroy K. Learning constitutive models from microstructural simulations via a non-intrusive reduced basis method. *Comput. Method. Appl. M.* 2021; 384: 113924. doi: 10.1016/j.cma.2021.113924
9. Gitman I. *Representative volumes and multi-scale modelling of quasi-brittle materials*. dissertation. Technische Universiteit Delft, Delft, The Netherlands; 2006.
10. Gitman I, Askes H, Sluys L. Representative volume: Existence and size determination. *Eng. Fract. Mech.* 2007; 74(16): 2518-2534. doi: 10.1016/j.engfracmech.2006.12.021
11. Hughes TJ. Multiscale phenomena: Green's functions, the Dirichlet-to-Neumann formulation, subgrid scale models, bubbles and the origins of stabilized methods. *Comput. Method. Appl. M.* 1995; 127(1-4): 387-401. doi: 10.1016/0045-7825(95)00844-9
12. Hughes TJ, Feijóo GR, Mazzei L, Quincy JB. The variational multiscale method—a paradigm for computational mechanics. *Comput. Method. Appl. M.* 1998; 166(1-2): 3-24. doi: 10.1016/s0045-7825(98)00079-6
13. Hou TY, Wu XH. A Multiscale Finite Element Method for Elliptic Problems in Composite Materials and Porous Media. *J. Comput. Phys.* 1997; 134(1): 169-189. doi: 10.1006/jcph.1997.5682
14. Larson MG, Målqvist A. Adaptive Variational Multiscale Methods Based on A Posteriori Error Estimation: Duality Techniques for Elliptic Problems. In: Springer-Verlag. 2005 (pp. 181-193)
15. Larson MG, Målqvist A. Adaptive variational multiscale methods based on a posteriori error estimation: Energy norm estimates for elliptic problems. *Comput. Method. Appl. M.* 2007; 196(21-24): 2313-2324. doi: 10.1016/j.cma.2006.08.019
16. Larson MG, Målqvist A. An adaptive variational multiscale method for convection-diffusion problems. *Commun. Numer. Meth. Engng.* 2009; 25(1): 65-79. doi: 10.1002/cnm.1106
17. Målqvist A, Peterseim D. Localization of elliptic multiscale problems. *Math. Comp.* 2014; 83(290): 2583-2603. doi: 10.1090/s0025-5718-2014-02868-8
18. Altmann R, Henning P, Peterseim D. Numerical homogenization beyond scale separation. *Acta Numer.* 2021; 30: 1-86. doi: 10.1017/s0962492921000015
19. Hesthaven JS, Rozza G, Stamm B. *Certified Reduced Basis Methods for Parametrized Partial Differential Equations*. SpringerBriefs in Mathematics Springer International Publishing . 2016
20. Quarteroni A, Manzoni A, Negri F. *Reduced Basis Methods for Partial Differential Equations*. 92 of UNITEXT - La Matematica per il 3+2. Cham: Springer International Publishing . 2016
21. Prud'homme C, Rovas D, Veroy K, et al. Reliable Real-Time Solution of Parametrized Partial Differential Equations: Reduced-basis Output Bound Methods. *J. Fluids Eng.* 2001; 124(1): 70-80. doi: 10.1115/1.1448332
22. Veroy K, Prud'homme C, Rovas D, Patera A. A Posteriori Error Bounds for Reduced-Basis Approximation of Parametrized Noncoercive and Nonlinear Elliptic Partial Differential Equations. In: AIAA. American Institute of Aeronautics and Astronautics; 2003: 2003-3847

23. Holmes P, Lumley JL, Berkooz G, Rowley CW. *Turbulence, Coherent Structures, Dynamical Systems and Symmetry*. Cambridge Monographs on Mechanics Cambridge University Press . 2009
24. Kunisch K, Volkwein S. Galerkin Proper Orthogonal Decomposition Methods for a General Equation in Fluid Dynamics. *SIAM J. Numer. Anal.* 2002; 40(2): 492-515. doi: 10.1137/s0036142900382612
25. Barrault M, Maday Y, Nguyen NC, Patera AT. An ‘empirical interpolation’ method: Application to efficient reduced-basis discretization of partial differential equations. *Cr. Math.* 2004; 339(9): 667-672. doi: 10.1016/j.crma.2004.08.006
26. Chaturantabut S, Sorensen DC. Nonlinear Model Reduction via Discrete Empirical Interpolation. *SIAM J. Sci. Comput.* 2010; 32(5): 2737-2764. doi: 10.1137/090766498
27. Ryckelynck D. A priori hyperreduction method: An adaptive approach. *J. Comput. Phys.* 2005; 202(1): 346-366. doi: 10.1016/j.jcp.2004.07.015
28. Ryckelynck D. Hyper-reduction of mechanical models involving internal variables. *Int. J. Numer. Meth. Engng* 2009; 77(1): 75-89. doi: 10.1002/nme.2406
29. Farhat C, Avery P, Chapman T, Cortial J. Dimensional reduction of nonlinear finite element dynamic models with finite rotations and energy-based mesh sampling and weighting for computational efficiency. *Int. J. Numer. Meth. Engng* 2014; 98(9): 625-662. doi: 10.1002/nme.4668
30. Farhat C, Chapman T, Avery P. Structure-preserving, stability, and accuracy properties of the energy-conserving sampling and weighting method for the hyper reduction of nonlinear finite element dynamic models. *Int. J. Numer. Meth. Engng* 2015; 102(5): 1077-1110. doi: 10.1002/nme.4820
31. Hernández J, Caicedo M, Ferrer A. Dimensional hyper-reduction of nonlinear finite element models via empirical cubature. *Comput. Method. Appl. M.* 2017; 313: 687-722. doi: 10.1016/j.cma.2016.10.022
32. Guo M, Hesthaven JS. Reduced order modeling for nonlinear structural analysis using Gaussian process regression. *Comput. Method. Appl. M.* 2018; 341: 807-826. doi: 10.1016/j.cma.2018.07.017
33. Raissi M, Perdikaris P, Karniadakis G. Physics-informed neural networks: A deep learning framework for solving forward and inverse problems involving nonlinear partial differential equations. *J. Comput. Phys.* 2019; 378: 686-707. doi: 10.1016/j.jcp.2018.10.045
34. Buhr A, Iapichino L, Ohlberger M, Rave S, Schindler F, Smetana K. *6 Localized model reduction for parameterized problems*: 245–306; De Gruyter . 2020
35. Babuška I, Lipton R. Optimal Local Approximation Spaces for Generalized Finite Element Methods with Application to Multiscale Problems. *Multiscale Model. Simul.* 2011; 9(1): 373-406. doi: 10.1137/100791051
36. Smetana K, Patera AT. Optimal Local Approximation Spaces for Component-Based Static Condensation Procedures. *SIAM J. Sci. Comput.* 2016; 38(5): A3318-A3356. doi: 10.1137/15m1009603
37. Buhr A, Smetana K. Randomized Local Model Order Reduction. *SIAM J. Sci. Comput.* 2018; 40(4): A2120-A2151. doi: 10.1137/17m1138480
38. Iapichino L, Quarteroni A, Rozza G. Reduced basis method and domain decomposition for elliptic problems in networks and complex parametrized geometries. *Comput. Math. Appl.* 2016; 71(1): 408-430. doi: 10.1016/j.camwa.2015.12.001
39. Babuška I, Caloz G, Osborn JE. Special Finite Element Methods for a Class of Second Order Elliptic Problems with Rough Coefficients. *SIAM J. Numer. Anal.* 1994; 31(4): 945-981. doi: 10.1137/0731051
40. Babuška I, Melenk J. The Partition Of Unity Method. *Int. J. Numer. Meth. Engng.* 1997; 40(4): 727-758. doi: 10.1002/(sici)1097-0207(19970228)40:4<727::aid-nme86>3.0.co;2-n
41. Babuška I, Banerjee U, Osborn JE. Generalized Finite Element Methods — Main Ideas, Results And Perspective. *Int. J. Comput. Methods* 2004; 01(01): 67-103. doi: 10.1142/s0219876204000083

42. Zienkiewicz O, Taylor R. *The Finite Element Method Volume 1: The Basis*. Oxford: Butterworth-Heinemann. 5th ed. 2000.
43. Bertram A, Glüge R. *Solid Mechanics*. Springer International Publishing . 2015
44. Milk R, Rave S, Schindler F. pyMOR – Generic Algorithms and Interfaces for Model Order Reduction. *SIAM J. Sci. Comput.* 2016; 38(5): S194-S216. doi: 10.1137/15m1026614
45. Sirovich L. Turbulence and the dynamics of coherent structures. I. Coherent structures. *Quart. Appl. Math.* 1987; 45(3): 561-571. doi: 10.1090/qam/910462
46. Unger JF, Eckardt S. Multiscale Modeling of Concrete. *Arch Computat Methods Eng* 2011; 18(3): 341-393. doi: 10.1007/s11831-011-9063-8
47. Lee NS, Bathe KJ. Effects of element distortions on the performance of isoparametric elements. *Int. J. Numer. Meth. Engng.* 1993; 36(20): 3553-3576. doi: 10.1002/nme.1620362009
48. Amsallem D, Zahr MJ, Farhat C. Nonlinear model order reduction based on local reduced-order bases. *Int. J. Numer. Meth. Engng* 2012; 92(10): 891-916. doi: 10.1002/nme.4371
49. Schettino EN. pydoit/doit: task management & automation tool (python). <https://doi.org/10.5281/zenodo.4892136>; 2021
50. Diercks P, Veroy K, Robens-Radermacher A, Unger JF. Multiscale modeling of linear elastic heterogeneous structures based on a localized model order reduction approach. <https://arxiv.org/abs/2201.10374>; 2022.
51. Alnæs MS, Blechta J, Hake J, et al. The FEniCS Project Version 1.5. *Archive of Numerical Software* 2015; 3(100). doi: 10.11588/ans.2015.100.20553

How to cite this article: P. Diercks, K. Veroy, A. Robens-Radermacher, and J. F. Unger (2022), Multiscale modeling of linear elastic heterogeneous structures via localized model order reduction, *International Journal for Numerical Methods in Engineering*, 2022;XX:X-X.